Geometric flow control in lateral flow assays: Macroscopic two-phase modeling

Farshid Jamshidi,[1,2,a)] Siamak Bayat,[1,2] Andrea Ernst,[3] and Britta Nestler[1,2]

AFFILIATIONS

[1]Institute of Digital Materials Science (IDM), Karlsruhe University of Applied Sciences, Moltkestraße 30, 76133 Karlsruhe, Germany

[2]Institute for Applied Materials - Microstructure Modelling and Simulation (IAM-MMS), Karlsruhe Institute of Technology (KIT), Straße am Forum 7, 76131 Karlsruhe, Germany

[3]Sartorius Stedim Biotech GmbH, August-Spindler-Straße 11, 37079 Göttingen, Germany

[a)]**Author to whom correspondence should be addressed:** farshid.jamshidi@h-ka.de

ABSTRACT

Lateral flow assays (LFAs) are widely employed in a diverse range of applications, including clinical diagnostics, pharmaceutical research, forensics, biotechnology, agriculture, food safety, and environmental analysis. A pivotal component of LFAs is the porous polymeric membrane, which facilitates the capillary-driven movement of fluids, known as "imbibition," in which a wetting fluid displaces a non-wetting fluid within the pore space of the membrane. This study presents a multi-scale modeling framework designed to investigate the imbibition process within LFAs. The framework integrates microscopic membrane characteristics into a macroscopic two-phase flow model, allowing the simulation of imbibition in membranes with different micro-scale properties and macro-scale profiles. The validity of the model was established through comparative analysis with documented case studies, a macro-scale single-phase flow model, and experimental observations, demonstrating its accuracy in simulating the imbibition process. The study also examines imbibition in various geometric configurations, including bifurcated (Y-shaped) and multi-branch geometries commonly found in multiplexed LFAs. The influence of geometric features such as length ratio, width ratio, branching angle, bifurcation point location, and asymmetry on fluid transport is investigated. Results indicate that membranes with larger branching angles exhibit slower imbibition. In addition, the influence of membrane type on macroscopic flow patterns is evaluated, showing that membranes with lower permeability require longer imbibition times. The insights gained from this research support a data-driven strategy for manipulating wetting behavior within LFAs. This approach can be leveraged to optimize the performance of LFAs and increase their effectiveness in various applications.

I. INTRODUCTION

In the medical field, rapid diagnostic tests are crucial, especially in urgent care scenarios or in settings where resources are limited. A prominent variant of such tests is the lateral flow assay (LFA), which is based on antigen identification.[1] The attributes of convenience, portability, rapid response, and increased sensitivity make LFAs an indispensable tool for point-of-care testing. As a result, LFAs have gained widespread acceptance for the diagnosis of various conditions, including pregnancy and infectious diseases, such as coronavirus disease 2019 (COVID-19). This manuscript focuses on a key component within LFAs: the cellulose nitrate (CN) membrane, a widely used polymeric porous material. We investigate the capillary-driven fluid dynamics within these membranes, as this phenomenon governs the movement of the sample liquid through the LFA and ultimately dictates the functionality of the assay.

A thorough understanding of fluid migration in CN membranes is crucial for optimizing LFA performance. The introduction of a membrane into a liquid reservoir initiates the movement of liquid within the pore space of the membrane, a phenomenon known in scientific terms as wicking or imbibition. This process in LFAs, driven solely by surface tension forces, eliminates the need for auxiliary driving mechanisms, making the technology particularly interesting. The wicking action is critical to the transport of the sample fluid and facilitates interaction with the bioreceptors attached to the membrane. The manifestation of a positive test result, marked by a visual color indicator in an LFA, arises from the specific binding of the target analyte to its corresponding antibodies, forming a complex that accumulates at the test zone.

A primary challenge in the development of LFAs is the need for multiplexed detection, where multiple analytes must be accurately identified for effective diagnosis.[2] Multiplexed testing, which involves the simultaneous detection of multiple biomarkers, plays a pivotal role in modern clinical diagnostics. It offers a more comprehensive understanding of disease states, reduces the risk of false positives and negatives, and enhances diagnostic accuracy. Furthermore, multiplexed testing can significantly reduce diagnostic time and cost compared to performing multiple individual tests. One type of such assay is multiplexed lateral flow biosensors. These have emerged as promising candidates for point-of-care diagnostics and are well aligned with the ASSURED (affordable, sensitive, specific, user-friendly, rapid/robust, equipment-free, and deliverable to end-users) criteria.[3] In addition to clinical diagnostics, a variety of other fields, such as forensics, food safety control, and environmental analysis, are increasingly requiring the concurrent measurement of multiple substances from a single sample.[4] This growing demand for multiplexing arises from the inadequacy of a single biomarker to provide comprehensive information.

To improve detection efficiency, significant efforts have been invested in the development of multiplexed LFAs. These efforts have resulted in two primary strategies:[4] (i) Device architecture modification: Modifying the physical design of the LFA to accommodate multiple detection zones or channels. (ii) Probe-based multiplexing: Using different types of probes or tags to distinguish between multiple analytes within a single LFA. In this study, the term “multiplexed LFA” refers to the first group, which includes multiple pathways (different test and control lines within each pathway) for a single sample. This configuration allows several analytes to be tested concurrently within one run. The architecture of multiplexed LFAs has a significant impact on fluid flow dynamics. The design of multiplexed LFAs determines how the fluid moves along different pathways, affecting the detection and analysis of analytes within each pathway.

The velocity of the sample fluid traversing the membrane significantly influences the manifestation and timing of a positive test result. This velocity must fall within a specific range to allow the necessary biorecognition events (i.e., antibody-analyte binding) to occur effectively. Flow rates exceeding this optimal range can hinder these reactions, leading to a false negative result despite the presence of the target analyte. Conversely, excessively slow flow rates may still yield a positive test; however, the visual color signal may be significantly delayed or prolonged. Therefore, careful regulation of the flow rate through the membrane is essential for optimal LFA performance.

The exploration and advancement of LFAs are underpinned by two principal methodologies: experimental and modeling approaches. Traditional methods focus largely on macro-scale experimentation, while contemporary strategies combine mathematical modeling with computational simulations. The former requires state-of-the-art infrastructure for reliable results, while the latter relies primarily on computational resources, offering potential reductions in cost and time compared to experimental modalities. In addition, it mitigates the propensity for measurement inaccuracies attributable to human or instrumental variables.

Numerical simulations are an invaluable tool for elucidating and refining the functionality of LFA. This approach involves a high-fidelity reconstruction of the intricate pore network within a porous membrane, enabling the application of computational fluid dynamics techniques. However, the simulation of fluid flow within porous membranes presents significant challenges. While suitable for the analysis of localized regions of interest, this method becomes computationally impractical for the analysis of wicking behavior over the entire LFA domain due to the large length scales involved (2–4 cm). Accurately representing the pore space necessitates an exponential increase in mesh cells, rendering the solution of governing equations (e.g., Stokes equations) intractable. To overcome these limitations, researchers often employ a homogenization approach. This method treats the entire LFA as a uniform porous continuum characterized by effective parameters. These parameters capture the collective influence of the intricate pore network at the macroscopic scale, providing a computationally tractable alternative for studying wicking phenomena within LFAs.

In our previous work,[5] we developed a macro-scale single-phase model to simulate liquid transport within axisymmetric LFAs with varying cross sections and a singular flow path. While the model accurately represents wicking phenomena, the mathematical computations become increasingly complex with more complicated geometries. To address this limitation, a new approach is required that can seamlessly accommodate a wider range of geometries. This model should be able to straightforwardly simulate wicking in all types of membrane profiles, such as the branched configurations used in multiplexed LFAs. Previous studies have explored imbibition dynamics in LFAs, including the study by Patari and Mahapatra[6] on the wicking phenomenon in filter paper substrates. Their study elucidated the physics behind the capillary rise of water in paper strips through various approaches, such as experimental investigations and simulation techniques. However, the focus remained solely on the rectangular profiles used in many practical applications.

Das *et al.*[7] further advanced this field by performing numerical simulations of wicking in membranes with varying cross sections. Their model facilitated the evaluation of optimal paper shapes and environmental conditions to maximize imbibition rates and minimize front broadening. However, their investigation was restricted to single flow path configurations.

Despite previous research advances, there remains a significant knowledge gap regarding the wicking behavior within multiplexed LFAs. This study seeks to address this deficiency by focusing on the fluid dynamics within these complex geometries, which have been inadequately explored. The complex network of flow paths in multiplexed LFAs influences the imbibition dynamics. To understand how fluid flows in different pathways, numerical simulations will be employed in this work. The outcomes of this research are expected to provide a more comprehensive understanding of LFA performance in multiplexed formats. This improved knowledge will contribute to the optimization of multiplexed LFA designs, potentially leading to improved sensitivity and overall assay performance. Moreover, the insights gained from this study have the potential to provide broader implications for the development of other microfluidic devices and paper-based diagnostic tools.

This paper presents a two-phase framework for simulating fluid movement through membranes at the macroscopic scale. We demonstrate the utility of this model with one-dimensional (1D) and two-dimensional (2D) simulations and show its ability to accurately represent the wicking process in LFAs. This two-phase approach addresses the limitations of the single-phase model by incorporating the complexities associated with fluid bifurcation and distribution in branched layouts. It is, therefore, suitable for a wider range of LFA designs. In addition, this model evaluates the effect of membrane morphology on liquid front dynamics, providing valuable insights for LFA design and optimization.

This paper is organized as follows. Section II details the structural and wetting properties of the membranes studied. It also provides a brief overview of the single-phase modeling framework established in our previous work. In this section, the developed two-phase wicking model and its validation strategy are further elaborated. Section III presents the results of this study. Finally, Sec. IV summarizes the main conclusions of our research.

II. MATERIALS AND METHODS

A. Porous membranes

This section begins with an examination of the structural characteristics of two different types of cellulose nitrate (CN) membranes. Following this characterization, the interactions between these membranes and two different liquids are investigated. The knowledge gained from these investigations will serve as the basis for the macroscale modeling described later in the paper.

1. Structural properties

Confocal laser scanning microscopy images of two different CN membrane types (A and B) were obtained from *Sartorius Stedim Biotech GmbH*. The image stack for membrane type A had a voxel resolution of 80 nm/voxel, while that of membrane type B had a coarser resolution of 160 nm/voxel. Following the methodology of Altschuh *et al.*,[8] three-dimensional digital representations (i.e., digital twins) of the membranes were constructed using the in-house software package PACE3D.[9] PACE3D, which stands for parallel algorithms for crystal evolution in three-dimension, is a modular software framework designed for large-scale parallel simulations of multi-component, multiphase, and polycrystalline materials undergoing phase transformations and microstructure evolution. The software incorporates a comprehensive suite of pre-processing and post-processing algorithms, including functionalities for porous media analysis.[10] To ensure consistency in the analysis, the reconstructed structural grid of type A was downsampled to match the lower resolution of type B (160 nm/voxel). This downsampling was achieved within PACE3D by combining adjacent cells in each spatial direction. Consequently, the resulting digital twins for type A and type B consisted of domains (in x, y, and z-directions) with dimensions $1020 \times 1020 \times 860$ and $620 \times 620 \times 880$ cells, respectively.

These reconstructed domains span the entire thickness of the membranes (in z-direction), approximately 140 μm. A pertinent question is whether this domain size is representative of the entire membrane. Altschuh[8] addressed this concern by performing a representative volume element (RVE) analysis. The purpose of the RVE analysis was to validate the adequacy of the microstructural detail captured in the images. Another objective was that analyzing larger sections would not add information. Considering the full membrane thickness, the RVE analysis determined a minimum length requirement of 36 μm in each remaining direction (x and y-directions). In this study, the shortest dimension of the reconstructed domains is approximately 100 μm, exceeding the established RVE length for CN membranes. Therefore, these digital twins can be considered as representative models for the entire membranes and are suitable for evaluation of porosity, permeability, and pore/ligament radius values derived from microstructure modeling described in Ref. 8. The obtained values for type A and type B membranes are summarized in Table I.

Porous media, such as type A and type B porous membranes, are often conceptualized as a collection of dimensionally similar, aligned capillary tubes to represent fluid motion in the pore space by motion within the tubes. By applying the Young–Laplace equation for a single tube to this conceptualization, we obtain the equation for a porous medium as

$$\Delta p_c = \frac{2\gamma_{LG} \cos\theta}{r_{eff}}, \tag{1}$$

where Δp_c represents the capillary pressure, γ_{LG} denotes the surface tension coefficient between the liquid (L) and gas (G) phases, θ is the contact angle, and r_{eff} stands for the "effective" capillary radius. While determining the radius of a single cylindrical capillary is straightforward, it presents a significant challenge within complex porous structures.[11,12] In this study, we use the method introduced by Altschuh *et al.*[13] to calculate the effective pore radius. This method relates geometric structure parameters to the effective capillary radius by

$$r_{eff} = CF(r_l, r_p) \cdot r_p, \tag{2}$$

where r_l and r_p are the ligament radius and pore radius, respectively. The correction factor, $CF(r_l, r_p)$, accounts for the combined influence of the ligament and pore radii. The correlation for $CF(r_l, r_p)$ was obtained by fitting it to simulation results of simplified structures, yielding[13]

$$CF(r_l, r_p) = \frac{1.98}{r_l/r_p} + 3.012. \tag{3}$$

Using the pore and ligament radii obtained from this investigation, the effective pore radii for type A and type B membranes are determined to be 24.4 and 19.2 μm, respectively.

2. Wetting properties

This section investigates the wetting characteristics of CN membranes obtained from *Sartorius*. A Newtonian fluid displaces the gas (air) present in the pore space of these membranes. The displacing fluids employed are water and an alternative liquid referred to as *Porefil*® from *Porometer*. The relevant density and viscosity properties of these fluids are summarized in Table II. CN

TABLE I. Properties of the reconstructed CN membranes from images provided by *Sartorius.*

Membrane	Porosity (%)	Mean pore radius (μm)	Mean ligament radius (μm)	Permeability (m^2)
Type A	90.6	2.45	0.70	$2.47 \times 10^{\ 12}$
Type B	81.7	2.29	0.85	$1.29 \times 10^{\ 12}$

TABLE II. Properties of the fluids involved in the wicking of CN membranes at 20 °C.[8]

Fluid	Density, ρ (kg m^{-3})	Viscosity, μ (kg m^{-1} s^{-1})
Air	1.0	1.76×10^{-5}
Water	998	1.0×10^{-3}
Porefil®	1800	2.2×10^{-3}

membranes are inherently hydrophobic. To facilitate fluid distribution within these membranes, surface tension reduction is achieved by surfactant pretreatment. This process, known as membrane impregnation, involves immersing the CN membrane in a surfactant bath.[8] In the absence of surfactants at the air–water interface, the surface tension remains at 0.072 Nm^{-1}. However, in the presence of surfactants within the CN membrane, the surface tension is reduced to 0.053 Nm^{-1}. For computational efficiency, the dynamic behavior of the contact angle during the imbibition process is intentionally neglected in this study. As reported in Ref. 8, experiments performed at *Sartorius* showed that the contact angle of water on an impregnated CN membrane is a static 36°. Similarly, *Porefil*® is assumed to have a constant surface tension coefficient of 0.016 Nm^{-1} with a contact angle of 0°.

B. Single-phase wicking model

The application of the capillary model to porous media can be achieved by drawing an analogy to a single capillary tube.[14] This analogy leads to

$$\underbrace{\frac{2\gamma_{\mathrm{LG}}\cos\theta}{r_{\mathrm{eff}}}}_{\text{Capillary}} = \underbrace{\rho\frac{d(l\dot{l})}{dt}}_{\text{Inertia}} + \underbrace{\frac{\varepsilon\mu l\dot{l}}{K}}_{\text{Friction}} + \underbrace{\rho g l}_{\text{Gravity}}, \tag{4}$$

where r_{eff} denotes the effective pore radius, ε represents the porosity, K stands for the permeability of the porous medium, μ is the fluid viscosity, ρ is the fluid density, g refers to the gravitational acceleration, l denotes the imbibition length, and t represents the imbibition time.

In scenarios dominated by viscous effects, where gravitational and inertial contributions are negligible, Eq. (4) can be simplified as[15]

$$\frac{2\gamma_{\mathrm{LG}}\cos\theta}{r_{\mathrm{eff}}} = \frac{\varepsilon\mu l\dot{l}}{K}. \tag{5}$$

This simplification leads to an expression of the liquid front height as

$$l(t) = \sqrt{\frac{4K\gamma_{\mathrm{LG}}\cos\theta}{\mu\varepsilon r_{\mathrm{eff}}}} \cdot t^{1/2}, \tag{6}$$

which results in $t(l) = \frac{1}{2}\xi_{\mathrm{eff}} l^2$ with $\xi_{\mathrm{eff}} = \mu\varepsilon/(K\Delta p_c)$ as the wicking coefficient and $\Delta p_c = 2\gamma_{\mathrm{LG}}\cos\theta/r_{\mathrm{eff}}$ as the capillary pressure.

When both viscous and gravitational effects play a significant role and cannot be neglected, the capillary model for porous media, based on Eq. (4), can be represented as

$$\frac{2\gamma_{\mathrm{LG}}\cos\theta}{r_{\mathrm{eff}}} = \frac{\varepsilon\mu l\dot{l}}{K} + \rho g l. \tag{7}$$

The solution to this equation is expressed in the form $l(t)$ with a Lambert function W and takes into account the effective parameters associated with porous materials

$$l(t) = \frac{1}{\chi_{\mathrm{eff}}}\left[1 + W\left(-e^{-1-\frac{\chi_{\mathrm{eff}}^2 t}{\xi_{\mathrm{eff}}}}\right)\right], \tag{8}$$

with

$$\chi_{\mathrm{eff}} = \frac{\rho g r_{\mathrm{eff}}}{2\gamma_{\mathrm{LG}}\cos\theta} \quad \text{and} \tag{9a}$$

$$\xi_{\mathrm{eff}} = \frac{\mu}{2\gamma_{\mathrm{LG}}\cos\theta}\frac{\varepsilon r_{\mathrm{eff}}}{K}. \tag{9b}$$

1. Previous study about a single-phase model

In our previous work,[5] we established a single-phase model for fluid flow dynamics in microfluidic devices based on Darcy's law, excluding gravitational effects. This law relates the superficial fluid velocity vector ($\mathbf{u}$) to the negative pressure gradient (∇p) and the dynamic viscosity (μ) via $\mathbf{u} = -(\mathbf{K}/\mu)\nabla p$. In this law, $\mathbf{K}$ represents the permeability tensor. The objective of the single-phase model was to elucidate fluid propagation in single-passage membranes with different cross-sectional areas. The investigation began with a rectangular profile, as shown in Fig. 1, referred to as the "straight membrane" and was subsequently extended to other membrane geometries, such as hexagonal, sand timer-shaped, and barbell-shaped profiles.

For the straight membrane, the cross-sectional area accessible to fluid flow, denoted by $A_1(x)$, remains constant throughout the membrane. Mathematically, this can be expressed as $A_1(x) = a_1 \cdot \eta_1 = A_1$, where a_1 and η_1 represent the constant width and thickness of the membrane, respectively. This constant area leads to a simplified expression for the wicking time in the straight membrane

$$t_1(l) = \xi_{\mathrm{eff}}\int_0^l A_1\left[\int_0^z \frac{dx}{A_1}\right]dz = \frac{1}{2}\xi_{\mathrm{eff}} l^2, \tag{10}$$

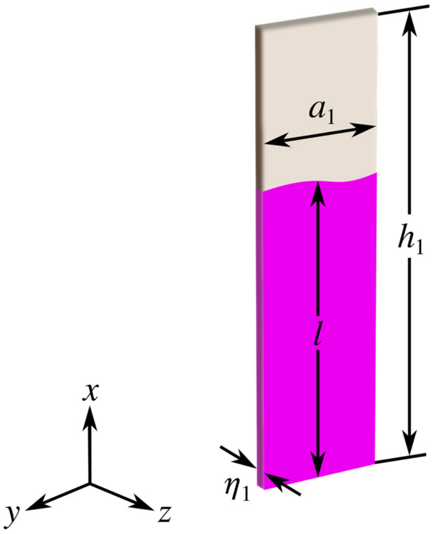

FIG. 1. Illustration of a straight membrane profile.

which is consistent with the result of Eq. (6). The single-phase model elucidates fluid propagation in single-passage, multi-segment membranes. Since the membrane thickness remains constant across all segments ($\eta_1 = \eta_2 = \eta_3$) and only the segment widths—labeled a_1, a_2, and a_3 in Fig. 2—vary, these segment widths represent the cross-sectional areas. Therefore, the wicking time in different segments can be expressed in terms of widths instead of areas as follows:

$$t_1 = \xi_{\mathrm{eff}} \int_0^l a_1(z) \left[\int_0^z \frac{dx}{a_1(x)} \right] dz, \tag{11a}$$

$$t_2 = \xi_{\mathrm{eff}} \int_{h_1}^l a_2(z) \left[\int_0^{h_1} \frac{dx}{a_1(x)} + \int_{h_1}^z \frac{dx}{a_2(x)} \right] dz, \tag{11b}$$

$$t_3 = \xi_{\mathrm{eff}} \int_{h_1+h_2}^l a_3(z) \left[\int_0^{h_1} \frac{dx}{a_1(x)} + \int_{h_1}^{h_1+h_2} \frac{dx}{a_2(x)} + \int_{h_1+h_2}^z \frac{dx}{a_3(x)} \right] dz. \tag{11c}$$

If the liquid front is within the first segment, the wicking time is calculated using Eq. (11a). If the liquid front reaches the second segment, Eq. (11b) is used to calculate the wicking time. When the liquid front is within the third segment, Eq. (11c) is employed to calculate the wicking time. Therefore, the wicking time in a membrane with three segments can be calculated as the sum of the wicking times for each segment, i.e., $t = t_1(h_1) + t_2(h_1 + h_2) + t_3(l)$. The single-phase model can be extended to calculate the wicking time in a membrane with n segments as $t = t_1(h_1) + t_2(h_1 + h_2) + t_3(h_1 + h_2 + h_3) + \cdots + t_n(l)$. To achieve $t_n(l)$ as the wicking time for the nth layer, $H_n = \sum_{m=0}^{n} h_m$ is defined as the cumulative length of n layers, where $H_0 = h_0 = 0$. Consequently, it can be written

$$t_n(l) = \xi_{\mathrm{eff}} \int_{H_{n-1}}^l a_n(z) \left[\left(\sum_{m=1}^{n-1} \int_{H_{m-1}}^{H_m} \frac{dx}{a_m(x)} \right) + \int_{H_{n-1}}^z \frac{dx}{a_n(x)} \right] dz. \tag{12}$$

Using the developed single-phase methodology, it is possible to predict the wicking time for a single-passage membrane consisting of multiple segments with arbitrary cross sections. A notable advantage of this approach is its simplicity compared to other methods that require the use of a mesh and the numerical solution of differential equations. Assuming that the determination of this integral is not complex, the main challenge is to find the wicking coefficient (ξ_{eff}). The elucidation of the wicking coefficient can be determined through two different approaches: (i) computational based on Eq. (9b), depending on the availability of microstructural evaluation, and (ii) experimental based on fitting Eq. (10) with experimental data, depending on the availability of experimental data.

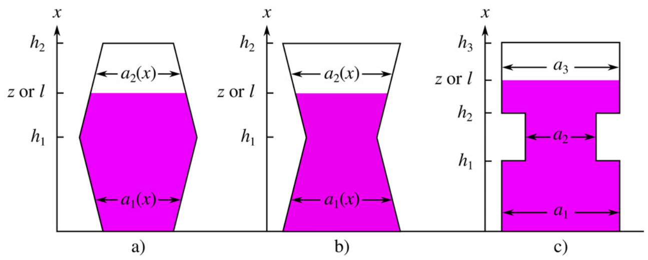

FIG. 2. Illustration of the membrane profiles: (a) hexagonal, (b) sand timer-shaped, and (c) barbell-shaped configuration.

C. Two-phase wicking model

The single-phase model simplifies the penetration process by assuming an initially empty pore space. While this approach offers computational advantages, it deviates from real-world scenarios where the pore space is occupied by an initial fluid. This necessitates the displacement of the incumbent (pre-existing) fluid by an invading liquid during the wicking process. To address this limitation, we present a macro-scale two-phase flow model that captures the displacement phenomenon in LFAs. This model considers two distinct fluid phases: (i) Incumbent non-wetting phase (index n): This phase, usually air, initially occupies the pore space and exhibits weaker interactions with the porous structure. (ii) Invading wetting phase (index w): This phase, such as water or a proprietary liquid like *Porefil*®, displaces the incumbent phase due to its favorable interactions with the porous media.

To distinguish between the two phases in two-phase flow through porous media, we use the parameter saturation (S), which quantifies the relative volume occupied by a given fluid phase within the pore space. Mathematically, the saturation of phase α (either non-wetting or wetting phase) is defined as

$$S_\alpha = \frac{V\!\!\!/_\alpha}{V\!\!\!/_{\mathrm{p}}} \quad \alpha = \mathrm{n},\ \mathrm{w}, \tag{13}$$

where $V\!\!\!/_\alpha$ represents the volume of the pore space occupied by the phase α and $V\!\!\!/_{\mathrm{p}}$ denotes the total volume of the pore space. Since the entire pore space is occupied by the two phases together, the saturation of each phase (S_{n} and S_{w}) inherently ranges from zero (no phase present) to one (entire pore space occupied). Consequently, the sum of the saturations of both phases is equal to one

$$S_{\mathrm{n}} + S_{\mathrm{w}} = 1. \tag{14}$$

The primary objective of the two-phase flow model in this study is to investigate the wicking process within a porous membrane in LFAs. For this purpose, the spatial distribution of fluid saturation throughout the wicking process is to be captured. In the context of two immiscible and incompressible fluids occupying a porous medium, saturation values quantify the "wetting state" of the membrane. These values indicate whether a given location within the membrane is completely wetted, partially saturated by the invading fluid, or completely dry. Since the model treats both fluids (e.g., air and water) as continuous phases at the macro-scale, a completely wetted membrane corresponds to a non-wetting phase saturation (S_{n}) of zero and a wetting phase saturation (S_{w}) of one. Conversely, a dry membrane is characterized by S_{n} equal to one and S_{w} equal to zero. Notably, non-zero values for both saturations can only occur simultaneously at the interface between the two fluid phases. This work focuses on resolving the evolving spatial distribution of wetting and non-wetting phase saturations within the porous membrane (i.e., the saturation field). By solving for this dynamic saturation field, we aim to demonstrate the ability of the model to accurately capture the movement of the liquid front throughout the membrane.

In two-phase flow through porous media, where the fluids are considered incompressible and immiscible, the mass balance equation governs the evolution of saturation for each phase (α). This can be expressed mathematically as

$$\varepsilon\frac{\partial S_\alpha}{\partial t} + \nabla\cdot\mathbf{u}_{\boldsymbol{\alpha}} = q_\alpha \quad \alpha = \mathrm{n},\ \mathrm{w}, \tag{15}$$

where ε represents the porosity of the medium, $\mathbf{u}_{\boldsymbol{\alpha}}$ is the velocity vector of the phase α, and q_α is the source/sink term. The velocity of each phase is determined by Darcy's law extended for two-phase flow as[16]

$$\mathbf{u}_\alpha = -\frac{k_{\mathrm{r}\alpha}\mathbf{K}}{\mu_\alpha}(\nabla p_\alpha - \rho_\alpha\mathbf{g}) \quad \alpha = \mathrm{n}, \mathrm{w}. \tag{16}$$

Compared to Darcy's law for single-phase flow ($\mathbf{u} = -(\mathbf{K}/\mu)\nabla p$) where gravitational effects are excluded, two important modifications are introduced in Eq. (16) for two-phase flow. The first modification concerns the concept of relative permeability. In single-phase flow, the permeability of the porous medium is a fixed property, represented by the absolute permeability ($\mathbf{K}$). In two-phase flow, however, the presence of one fluid can impede the movement of the other. To account for this interaction, the concept of relative permeability ($k_{\mathrm{r}\alpha}$) is introduced. Relative permeability depends on the saturation of both phases and reduces the effective permeability experienced by each fluid phase compared to absolute permeability. The product $k_{\mathrm{r}\alpha}\mathbf{K}$ is called the phase permeability for phase α. The ratio of the relative permeability to the viscosity of the phase α is defined as the "mobility", $\lambda_\alpha = k_{\mathrm{r}\alpha}/\mu_\alpha$.[17] Mobility is a critical parameter that determines the relative ease with which a given phase flows through the porous medium.[17] The second modification concerns the consideration of the effect of gravity.

In the two-phase model, capillary pressure refers to the pressure difference at the interface between two immiscible fluids. It can be expressed as the difference between the pressure of the non-wetting phase and the pressure of the wetting phase,[18]

$$p_\mathrm{c} = p_\mathrm{n} - p_\mathrm{w}. \tag{17}$$

Equations (14)–(17) represent the complete two-phase flow model in porous media. Only two variables among non-wetting phase saturation (S_n), wetting phase saturation (S_w), non-wetting phase pressure (p_n), and wetting phase pressure (p_w) can be selected as independent unknowns. This limitation arises because these variables are inherently linked through physical relationships. Different choices of independent variables lead to mathematically equivalent formulations describing the same physical phenomenon. This study adopts a formulation based on the non-wetting phase pressure (p_n) and the wetting phase saturation (S_w) as the primary unknowns for modeling immiscible two-phase flow. This choice implies the following relationships between the remaining variables: (i) Wetting phase pressure: According to Eq. (17), it is related to the non-wetting pressure and the capillary pressure: $p_\mathrm{w} = p_\mathrm{n} - p_\mathrm{c}$. (ii) Non-wetting phase saturation: Based on Eq. (14), it is related to the wetting phase saturation by the constraint of the total pore space occupancy: $S_\mathrm{n} = 1 - S_\mathrm{w}$.

By incorporating these dependencies and substituting Eq. (16) for the velocity terms in Eq. (15), the governing equations for the two-phase flow model are obtained as a system of partial differential equations[19]

$$-\varepsilon\frac{\partial S_\mathrm{w}}{\partial t} + \nabla\cdot\left(-\frac{k_\mathrm{rn}(S_\mathrm{w})\mathbf{K}}{\mu_\mathrm{n}}(\nabla p_\mathrm{n} - \rho_\mathrm{n}\mathbf{g})\right) = q_\mathrm{n}, \tag{18a}$$

$$\varepsilon\frac{\partial S_\mathrm{w}}{\partial t} + \nabla\cdot\left(-\frac{k_\mathrm{rw}(S_\mathrm{w})\mathbf{K}}{\mu_\mathrm{w}}(\nabla p_\mathrm{n} - \nabla p_\mathrm{c}(S_\mathrm{w}) - \rho_\mathrm{w}\mathbf{g})\right) = q_\mathrm{w}. \tag{18b}$$

By summing Eqs. (18a) and (18b), we can write

$$\begin{aligned}\nabla\cdot\Bigg(&-\frac{k_\mathrm{rn}(S_\mathrm{w})\mathbf{K}}{\mu_\mathrm{n}}(\nabla p_\mathrm{n} - \rho_\mathrm{n}\mathbf{g})\\ &-\frac{k_\mathrm{rw}(S_\mathrm{w})\mathbf{K}}{\mu_\mathrm{w}}(\nabla p_\mathrm{n} - \nabla p_\mathrm{c}(S_\mathrm{w}) - \rho_\mathrm{w}\mathbf{g})\Bigg) = q,\end{aligned} \tag{19}$$

where q is the total source/sink term, defined as $q = q_\mathrm{n} + q_\mathrm{w}$. In addition, the relative permeabilities and the capillary pressure are functions of S_w.

Based on Eq. (15) for the wetting phase saturation and Eq. (19) for the pressure equation, the final formulation of the two-phase system in porous media for two incompressible immiscible fluids in the (p_n, S_w) representation can be summarized as

$$\varepsilon\frac{\partial S_\mathrm{w}}{\partial t} + \nabla\cdot\mathbf{u}_\mathrm{w} = q_\mathrm{w}, \tag{20a}$$

$$\begin{aligned}-\nabla\cdot[\mathbf{K}(\lambda_\mathrm{n} + \lambda_\mathrm{w})\nabla p_\mathrm{n}] = q &- \nabla\cdot[\mathbf{K}(\lambda_\mathrm{n}\rho_\mathrm{n} + \lambda_\mathrm{w}\rho_\mathrm{w})\mathbf{g}]\\ &- \nabla\cdot(\mathbf{K}\lambda_\mathrm{w}\nabla p_\mathrm{c}),\end{aligned} \tag{20b}$$

where $\lambda_\mathrm{n} = k_\mathrm{rn}/\mu_\mathrm{n}$ and $\lambda_\mathrm{w} = k_\mathrm{rw}/\mu_\mathrm{w}$ represent the mobilities of the non-wetting and wetting phases, respectively. These are functions of S_w due to the dependency of the relative permeability on S_w. This equation system is fully coupled through Darcy velocity ($\mathbf{u}_\mathrm{w}$), which depends on the pressure and mobility [see Eq. (16)].

1. *Relative permeability and capillary pressure curves*

Understanding the dependence of relative permeabilities and capillary pressure on saturation allows the unknowns in Eqs. (20a) and (20b) to be reduced to S_w and p_n. This section introduces the concept of effective saturation to achieve this simplification. Then, a well-established correlation in the literature, the Brooks–Corey model, is presented to describe the influence of saturation on these parameters.

After the invasion of the wetting phase, a residual amount of the non-wetting phase remains trapped in the pore space, known as the residual non-wetting saturation (S_nr). Conversely, the residual wetting saturation (S_wr) represents the minimum wetting phase saturation that persists in the pores. The concept of effective saturation (S_eff) uses these residual saturations to specifically quantify the portion of the pore space that is actively contributing to the flow of the wetting phase. It is expressed mathematically as

$$S_\mathrm{eff} = \frac{S_\mathrm{w} - S_\mathrm{wr}}{1 - S_\mathrm{nr} - S_\mathrm{wr}}. \tag{21}$$

It is important to note that both saturation (S) and effective saturation (S_eff) are dimensionless quantities ranging from zero to one.

Brooks and Corey[20] proposed empirical correlations for relative permeability and capillary pressure based on experimental data from various rock formations. These correlations utilize effective saturation (S_{eff}), defined in Eq. (21), as the independent variable. The Brooks–Corey expressions for the relative permeabilities and capillary pressure are given by

$$k_{\mathrm{rn}}(S_{\mathrm{w}}) = k_{\mathrm{rn,\,max}}(1 - S_{\mathrm{eff}})^2\left(1 - S_{\mathrm{eff}}^{1+\frac{2}{b}}\right), \tag{22a}$$

$$k_{\mathrm{rw}}(S_{\mathrm{w}}) = k_{\mathrm{rw,\,max}} S_{\mathrm{eff}}^{3+\frac{2}{b}}, \tag{22b}$$

$$p_{\mathrm{c}}(S_{\mathrm{w}}) = p_{\mathrm{en}} S_{\mathrm{eff}}^{\frac{1}{b}}, \tag{22c}$$

where the pore size distribution index or exponent b typically has values between 0.2 and 3.0.[17] The maximum possible flow capacities for the non-wetting and wetting phases are given by the parameters $k_{\mathrm{rn,\,max}}$ and $k_{\mathrm{rw,\,max}}$, respectively. These values represent the maximum values of relative permeability that a fluid can reach under ideal conditions. In this case, ideal conditions are those in which a fluid is fully saturated within a particular range of pore sizes in the porous media, maximizing its ability to flow. This indicates full occupancy of the smaller pores for the wetting fluid and saturation of the larger pores for the non-wetting fluid.

The "entry pressure" in a porous medium, denoted by p_{en}, has a specific meaning in drainage processes involving the displacement of a liquid phase by a gas phase. As noted in Ref. 21, it is the lowest non-wetting phase pressure required to initiate invasion of a water-saturated porous medium. Imbibition processes—where a liquid phase displaces a gas phase—are not directly related to the idea of entry pressure. However, the capillary pressure is the macro-scale entry pressure in the Brooks–Corey model[6] and is intended to function as a macroscopic counterpart to the pore scale (micro-scale) entry pressure described by the Young–Laplace equation[22]

$$\text{Eq. (1)} \Rightarrow \mathrm{p_{en}} = \frac{2\gamma_{\mathrm{LG}}\cos\theta}{\mathrm{r_{eff}}}. \tag{23}$$

Using the concept of effective capillary pore radius, this method attempts to capture the effects of pore size phenomena on a larger scale within the porous material.

2. Initial and boundary conditions

The imbibition process in LFAs, characterized by a wetting liquid displacing a gas phase, can be simulated by solving the coupled system of Eqs. (20a) and (20b) for wetting phase saturation (S_{w}) and non-wetting phase pressure (p_{n}). This requires initial and boundary conditions. The initial condition for S_{w} is set to a very small value throughout the domain ($S_{\mathrm{w,\,initial}}$), mimicking a porous medium that is initially predominantly saturated with the non-wetting phase. A Dirichlet boundary condition (BC) is employed for the wetting phase saturation at the inlet. This is achieved by setting the saturation value to a fixed value ($S_{\mathrm{w,\,inlet}}$), which represents a constant inflow of wetting fluid from the liquid reservoir. A fixed pressure value ($p_{\mathrm{n,\,inlet}}$) is imposed at the inlet boundary for the non-wetting phase, corresponding to a Dirichlet BC. At the outlet, a Neumann BC is imposed on the wetting phase saturation. This implies that the normal derivative of S_{w} at the outlet is set to zero, implying no net wetting phase flow across the outlet. A Dirichlet BC is also used for the non-wetting phase pressure at the outlet where a fixed pressure ($p_{\mathrm{n,\,outlet}}$) is specified. Furthermore, q_{w} and q_{n} are set to zero, which means that no source/sink term (q) is considered.

3. Implicit pressure explicit saturation (IMPES) algorithm

The implicit pressure explicit saturation (IMPES) algorithm is widely used for simulating two-phase flow in porous media. This paper concisely overviews the IMPES approach, focusing on its core principles and numerical implementation details. The governing equations for the IMPES algorithm are presented in Eqs. (20a) and (20b) for saturation and pressure, respectively. The numerical discretization follows the work of Redondo *et al.*,[16] utilizing a second-order finite difference scheme for the spatial discretization.

Spatial discretization is implemented on a staggered Cartesian grid, with scalar quantities (saturation, pressure) evaluated at cell centers and vector quantities (velocities, gradients, mobilities) computed at midpoints between cell centers. The absolute permeability tensor is assumed to be isotropic and diagonal. Mobilities, which are functions of saturation, are calculated using a total variation diminishing (TVD) upwind scheme. This scheme minimizes numerical artifacts, particularly in scenarios with sharp saturation transitions, by prioritizing the flow direction and incorporating upstream information into the mobility calculations. Velocities are then determined using previously evaluated variables on the cell faces.

The core idea behind IMPES is the separation of pressure and saturation updates. As depicted in Fig. 3, the IMPES algorithm employed in this study and implemented in PACE3D[9] proceeds as follows:

1. The initial state and boundary conditions are defined. In the simulation, S_{w} and p_{n} represent scalar variables associated with a single cell, while $\mathbf{u}_{\mathrm{w}}$ is a vector variable. To denote variables for the entire computational domain, encompassing all cells, bold font notation is used.
2. Pressure ($\mathbf{p}_{\mathrm{n}}^{(n)}$) calculation: The non-wetting phase pressure equation [Eq. (20b)] is solved implicitly for the current time step denoted by the superscript (n). This equation is discretized into a system of linear equations with non-wetting phase pressure values as unknowns. This system can be expressed as $\mathbf{A}^{(n)}\mathbf{p}_{\mathrm{n}}^{(n)} = \mathbf{b}^{(n)}$, where $\mathbf{A}^{(n)}$ is the system matrix accounting for total transmissibilities [left side of Eq. (20b)], $\mathbf{p}_{\mathrm{n}}^{(n)}$ is the vector containing the non-wetting pressure at all points, and $\mathbf{b}^{(n)}$ includes terms related to flux sources, gravity, and capillary pressure [right side of Eq. (20b)]. Unlike Redondo *et al.*,[16] we use the biconjugate gradient stabilized (BiCGSTAB) method as the iterative solver for the non-wetting phase pressure equation.
3. Velocity ($\mathbf{u}_{\mathrm{w}}^{(n)}$) calculation: Pressure gradients are computed across each cell, and together with saturation-dependent mobilities, they determine the velocity field at the current time step.
4. The next time step, denoted as $t^{(n+1)}$, is calculated by summing the current time step ($t^{(n)}$) and the time interval (Δt).
5. The simulation ends when the specified simulation time is reached. If the desired simulation time is not attained, the process continues with further updates of the relevant fields.
6. Intermediate saturation ($\mathbf{S}_{\mathrm{w}}^{(n+1/2)}$) update: The saturation field, as governed by Eq. (20a), is explicitly updated for the first half of the time step ($\Delta t/2$) using the current velocity and current saturation values.

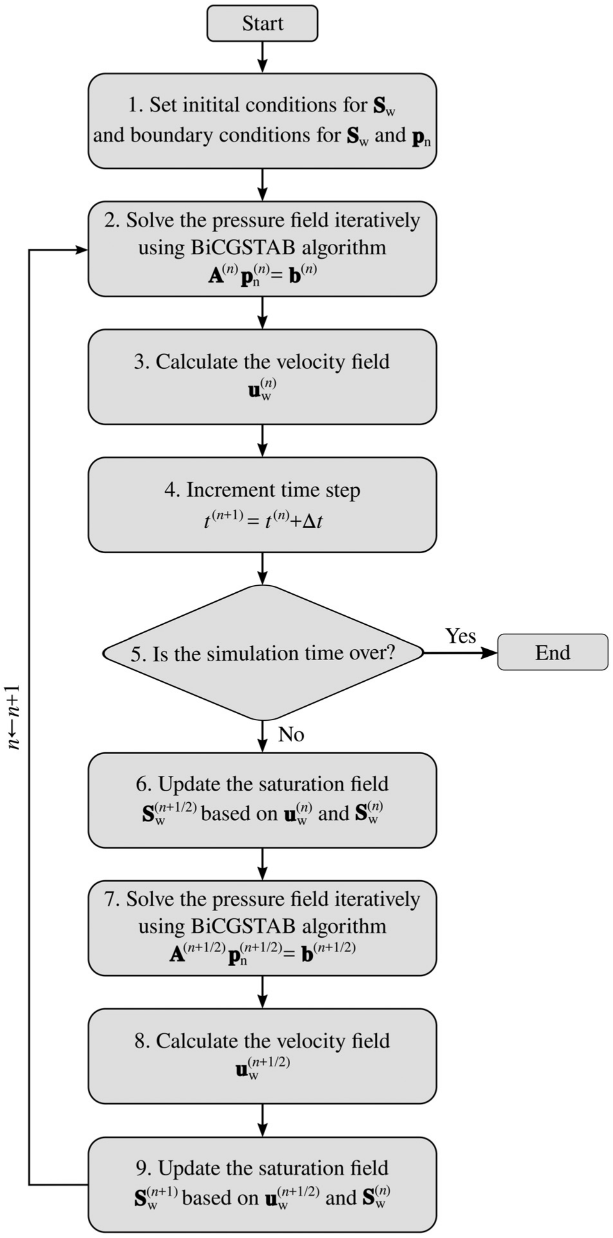

FIG. 3. The flow chart depicts the iterative solution procedure of the implicit pressure explicit saturation (IMPES) algorithm for two-phase flow simulations. Bold font indicates field variables.

7. Intermediate pressure ($\mathbf{p}_\mathrm{n}^{(n+1/2)}$) computation: The pressure field is updated based on the intermediate saturation values.
8. Intermediate velocity ($\mathbf{u}_\mathrm{w}^{(n+1/2)}$) calculation: The velocity field is updated based on the intermediate pressure gradients and mobilities. Using the intermediate velocity field improves the numerical stability of the algorithm.
9. Saturation ($\mathbf{S}_\mathrm{w}^{(n+1)}$) update: The wetting phase saturation equation [Eq. (20a)] is solved explicitly for the next time step, using the intermediate velocity field and current saturation values. The updated saturation field becomes the current reference state ($n \leftarrow n+1$). The entire process is then repeated from step 2.

4. Reliability assessment of the IMPES solver

This section focuses on the validation of the IMPES solver implemented in the PACE3D software environment for the simulation of imbibition processes. We evaluate the reliability of the solver by comparing its results with established benchmarks. First, the solver is validated through imbibition simulations using case studies documented in the literature. Second, we compare the results of wicking simulations from the two-phase model with those from a single-phase model and experimental data. This comparative analysis aims to determine the accuracy and capability of the solver to capture imbibition phenomena.

a. Validation. Altschuh *et al.*[13] investigated wicking in polymeric porous membranes using a two-phase phase-field approach to simulate wetting behavior within simplified representative structures. The simulation data were then employed to calculate the effective pore radius using Eqs. (2) and (3). Subsequently, the macro-scale flow model described by Eq. (8) was used to predict the wicking time in a straight membrane profile based on the calculated effective pore radius. Notably, the predicted wicking times exhibited good agreement with experimental data, highlighting the effectiveness of their approach. This methodology is referred to as a "semi-analytical solution" in this section due to its reliance on a simplified model for calculating the effective pore radius. Based on their experimental data and semi-analytical solution, this section aims to validate the implemented IMPES solver within PACE3D. The validation process leverages the parameters employed by Altschuh *et al.*[13] These specific parameters are summarized in Table III.

The wicking process is investigated through simulations of a straight (rectangular) membrane vertically positioned in a *Porefil*® reservoir. Due to a Bond number not significantly less than unity (detailed in Appendix A), the influence of gravity is included in the simulations. The gravitational acceleration vector is set to $\mathbf{g} = (0, -9.81, 0)^\mathrm{T}\ \mathrm{m\,s^{-2}}$. This inclusion is consistent with the semi-analytical solution, allowing a direct comparison between the simulation results and those obtained from both semi-analytical and experimental methods.

This approach focuses on two-phase flow simulations of wicking processes in distinct membrane profiles, which differs from the 1D single-phase model for unidirectional flow analysis within test strips. The two-phase model operates by discretizing the test strip profile. Straight membranes allow the representation of the computational domain in either one or two dimensions. Conversely, non-straight membranes, like those with a barbell-shaped profile, necessitate a 2D computational mesh to capture variations in the cross-sectional area accessible to the wicking liquid.

Wicking processes in two separate membrane types from Table III are simulated using the IMPES solver in PACE3D. For the investigated straight membrane, simulations are conducted using both a uniform 1D mesh containing 160 cells and a 2D mesh with dimensions of 100×160 cells. Both meshes yield a spatial resolution of 2.5×10^{-4} m. To ensure the accuracy of the solution, a TVD limiter with a small

TABLE III. Parameters used for the validation of the IMPES solver in PACE3D.

	Description	Value	
Parameter	Porous membrane	Type C	Type D
a_1	Width in horizontal direction (mm)	25	25
h_1	Length in vertical direction (mm)	40	40
ε	Porosity (%)	89	82
K	Permeability ($\times 10^{-12}$ m^2)	1.683	0.778
r_p	Mean pore radius (μm)	2.16	1.73
r_l	Mean ligament radius (μm)	0.64	0.72
	Non-wetting phase (air)		
μ_n	Viscosity (kg m^{-1} s^{-1})	1.76×10^{-5}	
ρ_n	Density (kg m^{-3})	1.0	
S_{nr}	Residual saturation (-)	0	
	Wetting phase (*Porefil*®)		
μ_w	Viscosity (kg m^{-1} s^{-1})	2.2×10^{-3}	
ρ_w	Density (kg m^{-3})	1800	
$S_{w,\,\mathrm{inlet}}$	Saturation at inlet (-)	1	
S_{wr}	Residual saturation (-)	0.01	
γ_{LG}	Surface tension coefficient (Nm^{-1})	0.016	
θ	Contact angle (°)	0	

value of 0.01 is implemented. The relative permeabilities are calculated using Eqs. (22a) and (22b), with both $k_{rn,\,\max}$ and $k_{rw,\,\max}$ set to unity.

Boundary conditions for the simulation are defined as follows: (i) at the inlet, $p_n = p_w + p_c = p_{atm} + p_c$ and $S_w = 1$, and (ii) at the outlet, $p_n = p_{atm} - \rho_n g h_1$. A Neumann boundary condition is imposed on S_w (zero-flux) at the outlet. (iii) On both sides of the 2D domain, Neumann boundary conditions are imposed for both p_n and S_w.

This case study employs the IMPES algorithm for solving the governing equations of two-phase flow in porous membranes [Eq. (20)]. The functions of relative permeabilities and capillary pressure based on effective saturation are established further using the Brooks–Corey model. When the effective saturation [defined by Eq. (21)] approaches zero, i.e., $S_w \rightarrow S_{wr}$, the relative permeability of the wetting phase also approaches zero ($k_{rw} \rightarrow 0$). Since relative permeability reflects a phase's ability to flow within the porous media, a zero value of k_{rw} signifies complete immobility for the wetting phase. This would effectively block the wetting phase flow. Moreover, this leads to unrealistically high capillary pressure values (approaching infinity) during the simulation. To mitigate these numerical instabilities, a threshold value for the wetting phase saturation is implemented. Accordingly, the computational domain is initially saturated with a wetting phase saturation of 0.011. This value is chosen to be close to the residual wetting phase saturation (S_{wr}), considering $S_{nr} = 0$.

The wetting phase commences its ascension from the reservoir through the pore space. In computational terms, $S_w = 1$ from the inlet upwards, progressively filling the cells initially containing $S_{w,\,\mathrm{initial}} = 0.011$. Once the wetting phase saturation surpasses the threshold of 0.011, the liquid front is considered to have reached that cell. Consequently, the foremost computational cell where S_w exceeds 0.011 is identified as the location of the liquid front.

To validate the implementation of the IMPES solver within the PACE3D software, this section utilizes a modified version of the capillary pressure derived from the Brooks–Corey model. This adjustment involves dividing the original capillary pressure equation [Eq. (22c)] by a factor of 1.4. While the unmodified Brooks–Corey model is commonly used for two-phase flow simulations in porous media, the modified version is employed here to achieve consistency when comparing the simulation results generated by the IMPES solver with the experimental data. It is important to distinguish that this adjustment is not intended to validate the Brooks–Corey model itself, but rather to facilitate a more effective validation of the solver's ability to capture the physics of the two-phase flow and wicking process within porous membranes. Hence, the following modified Brooks–Corey model is used for consistency in the remaining simulations presented in this study

$$k_{rn}(S_w) = (1 - S_{eff})^2 \left(1 - S_{eff}^{1+\frac{2}{b}}\right), \tag{24a}$$

$$k_{rw}(S_w) = S_{eff}^{3+\frac{2}{b}}, \tag{24b}$$

$$p_c(S_w) = \frac{1}{1.4} p_{en} S_{eff}^{-\frac{1}{b}}, \tag{24c}$$

with $b = 2$. Note that the entry pressure (p_{en}) is determined using Eq. (23). This equation incorporates the effective capillary radius, which is calculated based on Eqs. (2) and (3).

Figure 4 presents a comprehensive comparison between experimental observations and model predictions for wicking behavior in two distinct porous membrane types, designated as type C and type D. The experimental data points are represented by the symbols in the figure. Overlaid upon these data points are the curves depicting the predictions from both the semi-analytical method (represented by dashed lines) and the IMPES solver (represented by solid lines). The figure reveals a strong agreement between the model predictions and the experimental data for both porous membrane types.

A comparative analysis was performed to evaluate the performance of the semi-analytical solution and the IMPES simulation against experimental data. Percentage error analysis was applied using the experimental data as reference values for position measurements at different time points. The percentage error was calculated using

$$Error = \left| \frac{l - l_{Experiment}}{l_{Experiment}} \right| \cdot 100, \tag{25}$$

where l represents the predicted wicking length from one of the methods and $l_{Experiment}$ represents the wicking length from experiment 2. The average percentage error was calculated to provide a quantitative measure of the deviation of each method from the experimental data. The semi-analytical solution yielded an average percentage error of 18.85%, while the IMPES simulation achieved a lower average error of 15.70% for membrane type C. For membrane type D, these values were 14.78% and 10.03%, respectively.

This comparison shows that while both methods provide reasonable approximations to the experimental results, the IMPES simulations exhibit greater accuracy with lower errors compared to semi-analytical solutions. The reduced error of the IMPES solver suggests that the numerical simulation better captures the dynamics of the system under study and provides a closer representation of the experimental data for both membrane types. This observation provides

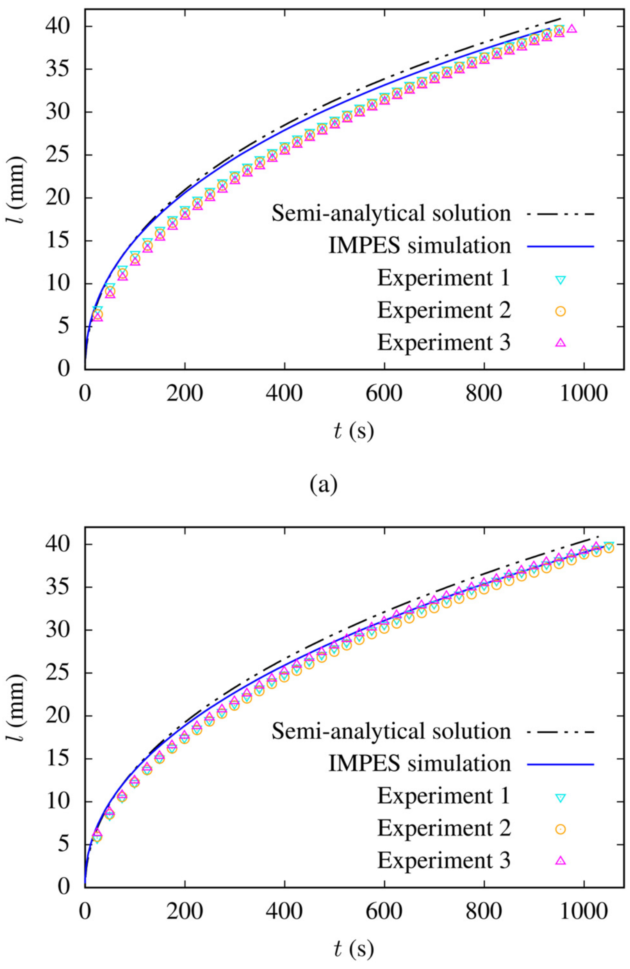

(a)

(b)

FIG. 4. Comparison of wicking curves for two porous membrane types: (a) type C and (b) type D. Solid lines represent the results of the IMPES solver (1D and 2D simulations). Experimental data are depicted by symbols, while dashed lines show the semi-analytical solutions from Ref. 13.

strong validation for the accuracy and effectiveness of the implemented IMPES solver in simulating wicking phenomena within porous membranes.

b. Comparison with the single-phase method. A macro-scale, single-phase model has been established to investigate the dynamics of liquid transport within lateral flow assays (LFAs). The primary objective of this model was to understand how variations in membrane geometry affect the wicking phenomenon. To isolate the geometrical effects, the model intentionally excluded membrane-related parameters (e.g., permeability) and fluid-related parameters (e.g., viscosity). These excluded effects were implicitly considered by calibrating Eq. (10) against experimental data obtained from a straight membrane.

While the single-phase model provided valuable insights, a two-phase approach, i.e., the IMPES simulation, is used in this section to consider the influence of microstructure characteristics and fluid properties. To perform a direct comparison between the two-phase and single-phase methods, four membrane profiles are chosen. These profiles have been previously investigated using the single-phase model and range from straight to hexagonal, sand-timer-shaped, and barbell-shaped profiles.

The IMPES simulation setup for this analysis builds upon the validation case with two key modifications: (i) Membrane type: Membrane type A (see Table I) is employed. In the experimental investigation and the single-phase model, in contrast, a *UniSart*®*CN 140 backed* membrane was utilized. (ii) Wetting phase properties: To maintain consistency with the experimental data and the single-phase model, water is chosen as the wetting phase. Its properties are detailed in Table II. This choice gives a surface tension coefficient (γ_{LG}) of $0.053\,\mathrm{N\,m^{-1}}$ and a contact angle (θ) of 36°.[8]

Figure 5 shows a comparison between the wicking curves predicted by both the single-phase model and the IMPES solver, along with experimental data for various membrane profiles. The observed good agreement between the predictions of the IMPES solver and the experimental data for all investigated membrane profiles indicates its ability to accurately capture the wicking behavior within these porous materials. This finding serves as a valuable validation of the effectiveness of the implemented IMPES solver in simulating wicking phenomena in LFAs.

The proposed approach in this section incorporates the influence of microstructural characteristics such as porosity and absolute permeability. In other words, it leverages micro-scale data within macro-scale simulations. Consequently, this methodology for investigating the wicking process in LFAs can be categorized as a multi-scale approach. The successful application of the IMPES solver to various cases in this section demonstrates its versatility and robustness in simulating fluid flow through different membrane types and configurations.

III. RESULTS AND DISCUSSION

A. Influence of geometry on wicking in multi-branch membranes

In this section, the IMPES solver is used to investigate the wicking process in multi-branch membranes. These geometries are characterized by the presence of multiple flow paths, allowing multiple experiments to be performed simultaneously, thereby increasing experimental throughput. By using the IMPES algorithm to simulate fluid flow within these structures, a more comprehensive understanding of wicking behavior in such complex geometries can be achieved.

The design of lateral flow assays (LFAs) can be guided by the principles of optimal flow configurations observed in nature, as embodied in the constructal law.[23,24] This law suggests that natural systems evolve toward configurations that promote optimal efficiency in transporting a fluid. Examples of this phenomenon can be seen in the tree-shaped structures of blood vessels, tree branches, and river basins. Motivated by this principle, numerous studies have explored the application of optimal design principles in branched flow networks.[25–29] These studies focus on minimizing the total hydraulic resistance within the network, taking into account factors such as individual segment geometry, branching patterns, number of branches, and material properties such as permeability. Typically, constraints are imposed on the network design, such as a fixed occupied area, volume, or total length.

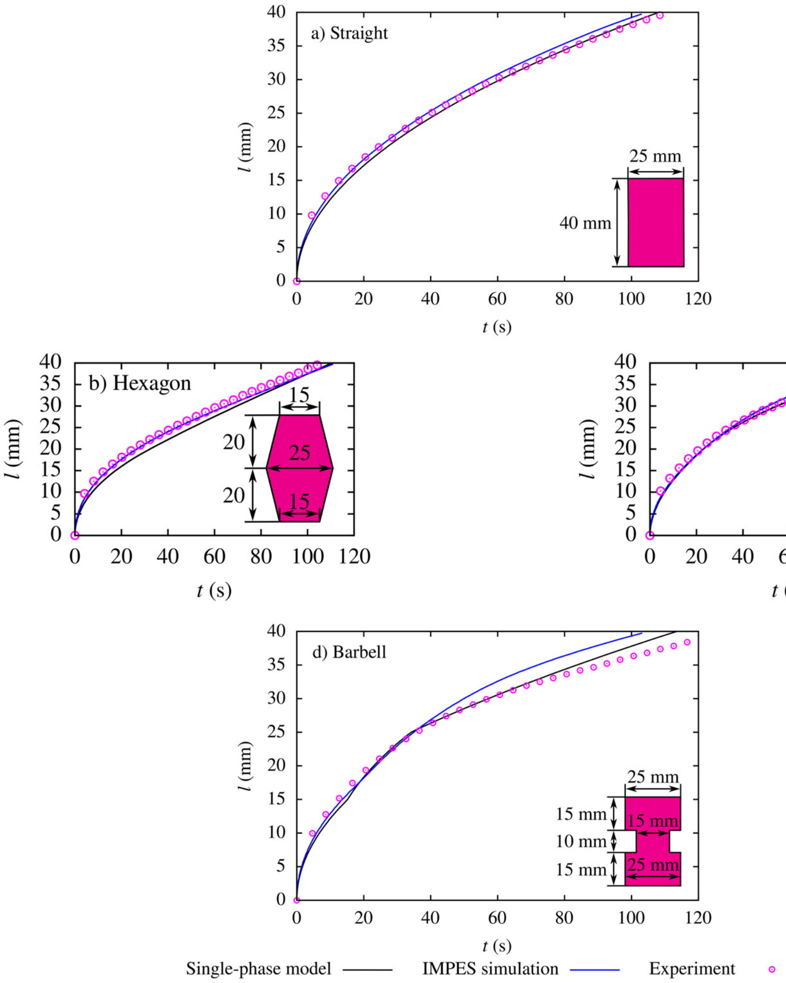

FIG. 5. Comparison of wicking curves for various membrane profiles: (a) straight, (b) hexagonal, (c) sand timer-shaped, and (d) barbell-shaped configuration. Results are presented for the single-phase model,[5] two-phase IMPES simulation, and experimental investigations.[5] Inset figures depict the dimensions of each profile in millimeters.

As documented in the literature, Lagrange multipliers can be used to derive optimal geometries that minimize flow resistance within these given constraints. This section explores the application of some of these optimized geometries as potential membrane profiles for LFA test strips.

1. Wicking in Y-shaped membranes

The initial exploration of multi-branch membranes commences with the simplest geometry: Y-shaped profiles, as shown schematically in Fig. 6. These profiles have a single level of bifurcation, which allows for the creation of two distinct fluid flow paths within the membrane. Assuming identical widths and lengths for the daughter segments, the geometry of the Y-shaped profile can be systematically varied by adjusting the following parameters: (i) Length ratio (l_2/l_1): This parameter is defined as the ratio of the length of a daughter segment (l_2) to the length of the first (main/parent) segment (l_1). (ii) Width ratio (a_2/a_1): This parameter represents the ratio between the width of a daughter segment (a_2) and the width of the first segment (a_1). (iii) Branching angle (δ): This parameter defines the angle formed between the two daughter segments.

The analysis of branching patterns has attracted significant scientific interest across both natural and engineered systems. The Hess–Murray law, named after Walter Rudolf Hess and Cecil Dunmore Murray, establishes a correlation between the radii of successive branches in bifurcating or trifurcating vessels observed in biological tissues.[30,31] This law is premised on minimizing the work required for blood or lymph circulation within living organisms. It defines an "optimal branching ratio" expressed as $r_{b+1}/r_b = 2^{\ 1/3} \approx 0.7937$ where the index b represents the bifurcation level, and r_b and r_{b+1} denote the radii of the parent and daughter vessels, respectively.

The Hess–Murray law has been rigorously reevaluated through extensive theoretical and experimental studies. These investigations have confirmed its validity under well-defined conditions, particularly for vessels with micro-scale radii. However, as evidenced by the research documented in Refs. 32 and 33, the applicability of the law diminishes for vessels with larger dimensions. While the Hess–Murray law offers a valuable "cubic root of 2" correlation for branching ratios, researchers have explored alternative configurations in the literature. Table IV summarizes these additional branching ratios and angles in addition to the Hess–Murray configuration.

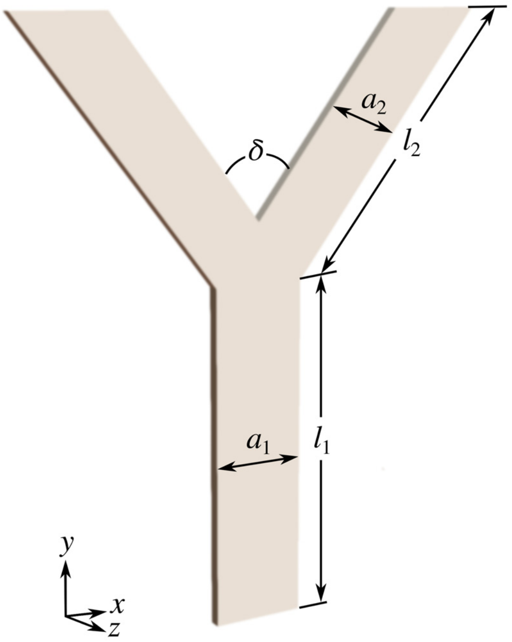

FIG. 6. Illustration of the membrane profile with a Y-shaped configuration.

The Y-shaped membrane profiles used in this study are derived from several sources, each offering a different perspective on optimal branching configurations. **Y1 profile** is adapted from the work of Shou *et al.*,[34] who investigated flow dynamics in tree-shaped networks. Their theoretical work aimed at designing the distribution of the radius and length of local branches to achieve the fastest capillary flow. **Y2 profile** originates from the reevaluation of the Hess–Murray law by Sciubba.[32] Sciubba proposed an alternative shape based on the functionality of the capillary network, suggesting that both the optimal bifurcation angle and the optimal radius ratio depend on the shape of the domain served by the bifurcation. **Y3 profile** is based on the Hess–Murray law and is consistent with the concept of maximum physical efficiency for connecting successive vessel segments. The size ratio is consistent with the law's suggestion for impermeable tree networks, as described by Miguel *et al.*[38] **Y4 profile** is adapted from examples in a study by Bejan and Lorente[35] who focused on optimizing the global performance of flow systems subject to global constraints. They assumed a constrained total volume occupied by the channels and sought to minimize the total flow resistance in the Y-shaped configuration. **Y5 profile** is derived from a study by Soni *et al.*,[36] which presents an analytical approach for both steady and unsteady flows. Their approach yielded optimal relationships for the homothetic ratio of tube sizes and optimal angles between daughter tubes. These optimal relationships satisfy the criterion of minimizing flow impedance, taking into account both geometry and svelteness ratio. **Y6 profile** is adapted from the work of Sehn *et al.*[37] who studied the laminar flow of non-Newtonian fluids in Y-shaped structures with varying ratios of parent and daughter tube sizes using numerical analysis.

TABLE IV. Length ratio (l_2/l_1), width ratio (a_2/a_1), and branching angle (δ) of Y-shaped membrane profiles.

Sample	l_2/l_1 (-)	a_2/a_1 (-)	δ (°)	From
Y1	0.4672	0.394	60	Ref. 34
Y2	0.567	0.433	60	Ref. 32
Y3	$2^{\frac{1}{3}} \approx 0.7937$	$2^{\frac{1}{3}} \approx 0.7937$	75	Refs. 30 and 31
Y4	1	$2^{\frac{3}{7}} \approx 0.743$	75	Ref. 35
Y5	$2^{\frac{1}{2}} \approx 0.707$	$2^{\frac{1}{4}} \approx 0.8409$	90	Ref. 36
Y6	0.8	0.8	135	Ref. 37

In contrast to the case studies using the 1D single-phase model, where the focus was on the wicking behavior within single-passage membranes, the two-phase approach investigates wicking in multi-passage (multi-branch) membranes. These membranes provide multiple paths for fluid flow, as exemplified by the Y-shaped profile where the flow splits into two daughter segments. Due to the significantly smaller thickness of the membrane in the *z*-direction compared to the other two spatial directions, the fluid motion within these Y-shaped profiles can be simulated using the 2D two-phase model. This is done using the validated IMPES solver implemented in the PACE3D software. Subsequently, a comparative analysis of the simulation results obtained for different Y-shaped configurations is performed to evaluate the influence of the aforementioned geometric parameters on the wicking behavior.

Y-shaped membrane profiles with dimensions given in Table IV are investigated using wicking simulations. These profiles possess an overall vertical length of 25±0.5 mm and a first segment width of 3.86 mm. The simulations employ an equidistant grid with a resolution of 7.9×10^{5} m. This resolution is determined to be sufficiently fine after a mesh independence study (not shown). Boundary conditions identical to those used in the validation case are applied to both the non-wetting phase pressure and the wetting phase saturation. Air and water are employed as the non-wetting and wetting phases, respectively, with their properties detailed in Table II. Residual saturations of 0 and 0.01 are assigned to the non-wetting and wetting phases, respectively, while the initial wetting phase saturation is set to 0.011. The TVD limiter is assigned a value of 0.01. Membrane type A, as described in Table I, is selected for the simulations.

Figure 7 presents the results for the wicking length as a function of time within the Y-shaped membranes. Due to the symmetric geometry of the profiles around the *y*-axis, the liquid front propagates identically in the two daughter segments. Consequently, the vertical coordinate of the liquid front within the first segment and subsequently within one of the daughter segments is monitored to represent the wicking length.

The results reveal a higher wicking velocity in the early stages of the process. All investigated geometries exhibit similar wicking behavior until the liquid front reaches their respective bifurcation points, which can vary in vertical position. Beyond these points, differences in the wicking curves become apparent. Notably, the wicking curves for Y-shaped membranes with identical branching angles remain closely aligned. Among the investigated geometries, the Y-shaped profile with a 60° branching angle from Ref. 34 exhibits the fastest imbibition, while the 135° Y-shaped membrane displays the slowest wicking time. In general, a longer wicking time is associated with a larger branching angle for Y-shaped membranes. This phenomenon can be explained by the constraint imposed on the total length in the *y*-direction. When considering a fixed vertical length for all Y-shaped geometries with comparable width ratios, a larger branching angle translates to a longer

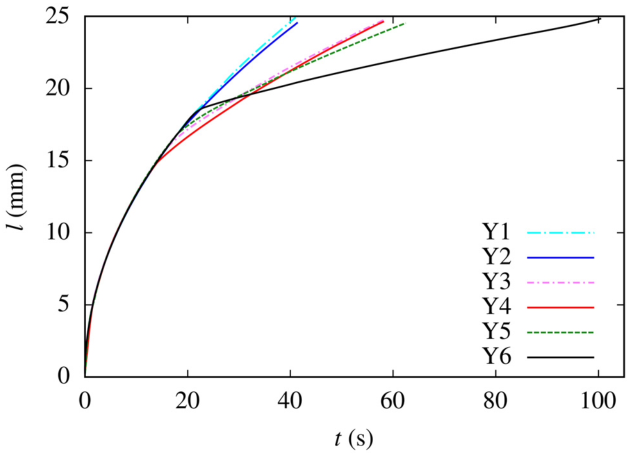

FIG. 7. Wicking length of water over time in Y-shaped membranes (profiles in Table IV).

TABLE V. Length ratio (l_{b+1}/l_b) and width ratio (a_{b+1}/a_b) between the $b+1$st branch and the bth branch and branching angle (δ_1 and δ_2) of tree-shaped membrane profiles.

Sample	l_{b+1}/l_b (-)	a_{b+1}/a_b (-)	δ_1 (°)	δ_2 (°)	From
Tree1	0.4799	0.4306	60	60	Ref. 34
Tree2	$2^{\frac{1}{3}} \approx 0.7937$	$2^{\frac{1}{3}} \approx 0.7937$	75	75	Refs. 30 and 31
Tree3	0.5	0.5	81.72	106.22	Ref. 39
Tree4	0.5	0.5	90	90	Ref. 39

path for the fluid to travel within the porous membrane, resulting in a longer wicking time.

Analogous to the observations made during the analysis of wicking in T-shaped membranes with expansions,[5] the presence of a junction in Y-shaped profiles leads to a decrease in wicking velocity within the subsequent segment. Another recurring wicking phenomenon observed in both T-shaped and Y-shaped profiles relates to the influence of earlier liquid entry into subsequent segments. As illustrated in Fig. 7, earlier entry into the second segment results in a steeper slope of the wicking curve, indicating a higher liquid velocity in that segment. Specifically, the wicking velocity observed in the second segment of the Y4 profile (solid red line) surpasses that of the Y6 profile (solid black line). Consequently, the liquid front in Y4 progresses faster, overtaking the liquid front in Y6. This translates to a slower overall wicking process in Y6 compared to Y4.

2. Wicking in membranes with four branches

This section investigates the wicking behavior within membranes characterized by two levels of bifurcation, forming a tree-shaped structure, as shown in Fig. 8(a). The dimensions of these tree-shaped membranes are obtained from the literature. In addition to the use of existing geometries, this study incorporates novel technology. *Sartorius* has developed a method for engraving various patterns into CN membranes. For the purposes of this study, *Sartorius* has kindly provided two membrane profiles from their multiplexed LFAs, as depicted in Figs. 8(b) and 8(c).

Tree-shaped flow networks with two bifurcation levels are characterized by the emergence of two daughter branches from a single parent branch at each bifurcation point in the subsequent level. The length and width ratios between these daughter and parent branches are expressed as l_{b+1}/l_b and a_{b+1}/a_b, respectively, where the index b ($b = 1, 2$) denotes the bifurcation level.

Natural systems exhibit characteristic size changes at vessel bifurcations. As documented by Miguel,[38] the ratio of successive lengths and diameters between daughter and parent vessels defines a scale factor, or homothetic ratio, independent of the specific bifurcation level (b). Notably, for laminar flow conditions, the Hess–Murray law proposes optimal length and width ratios of $2^{1/3}$ for ideal connections between parent and daughter vessels. This translates to a halving of diameters and lengths after every three successive branching generations. However, alternative configurations have been explored by researchers and may be more applicable in certain scenarios, as documented in the literature. Table V summarizes these alternative branching ratios and angles for tree-shaped membrane profiles (Tree1, Tree3, and Tree4), in addition to the configuration derived from the

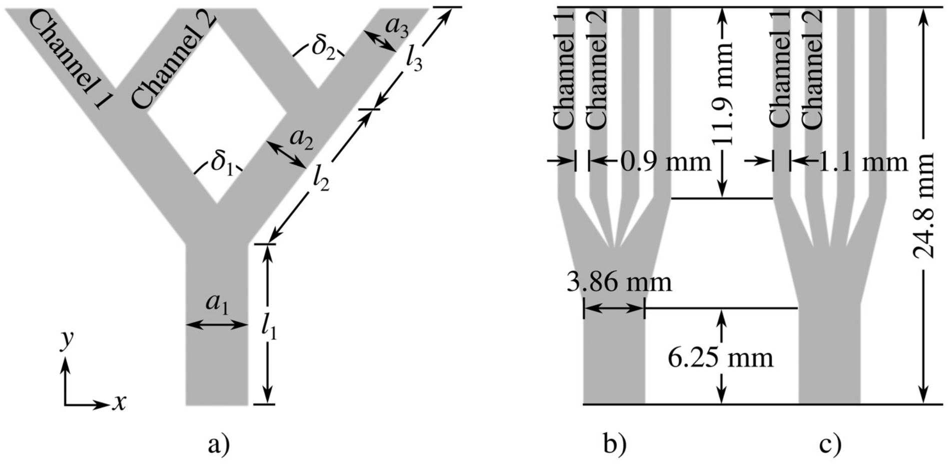

FIG. 8. Illustration of the membrane profile with four branches: (a) tree-shaped configuration; (b) *Sartorius* multiplex I, and (c) *Sartorius* multiplex II.

Hess–Murray law (Tree2). The wicking processes in tree-shaped membrane profiles with dimensions given in Table V and multiplexed membranes provided by *Sartorius* are studied using 2D simulations. All these profiles have a total vertical length of 25 ± 0.5 mm and a first segment width of $a_1 = 3.86\,\text{mm}$. The simulations are performed using the IMPES solver within the PACE3D software framework. An equidistant grid with a resolution of 7.9×10^{-5} m is used. Other simulation setups are similar to those employed for wicking in Y-shaped membranes.

Figures 9–11 present the wetting phase saturation profiles obtained from 2D simulations of wicking within the tree-shaped membrane (Tree2) based on the Hess–Murray law and within the multiplexed membranes designed by *Sartorius*. These figures serve to visualize the spreading behavior of the liquid. The evolution of the liquid interface within the remaining tree-shaped geometries listed in Table V is presented in Appendix B. The figures reveal a gradual diffusion of the liquid interface as it propagates throughout the domain.

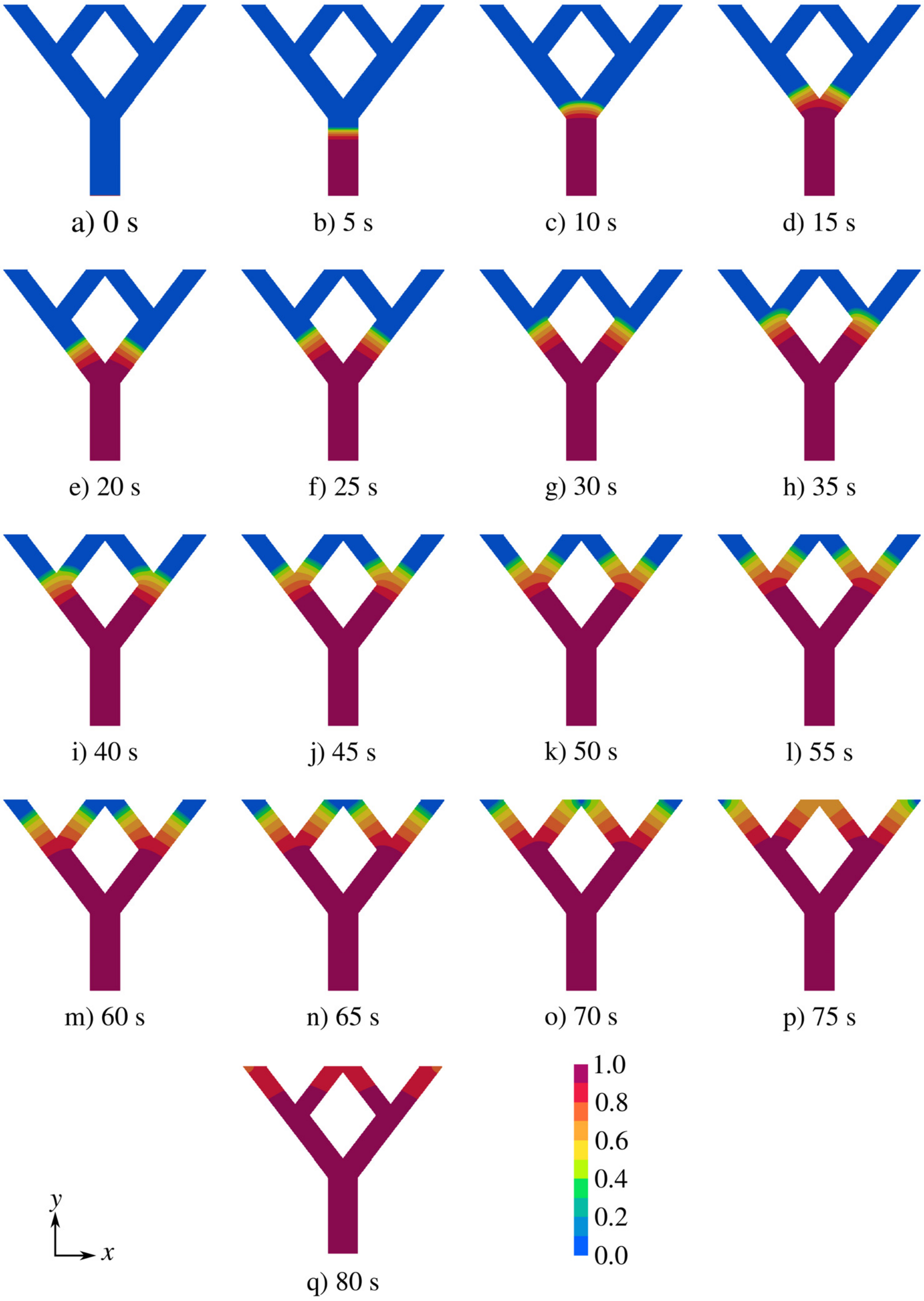

FIG. 9. The wetting phase (water) saturation in Tree2 membrane profile from Table V, where the evolution is displayed every 5 s.

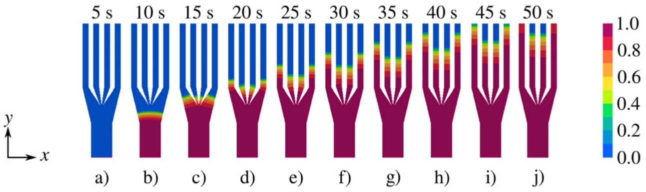

FIG. 10. The wetting phase (water) saturation in the multiplex I designed by *Sartorius*, where the evolution is displayed every 5 s.

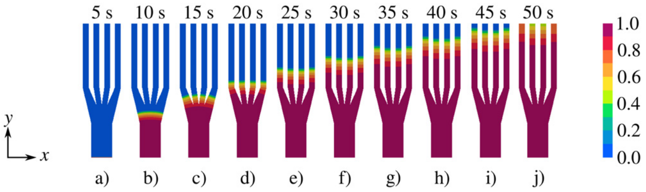

FIG. 11. The wetting phase (water) saturation in the multiplex II designed by *Sartorius*, where the evolution is displayed every 5 s.

This diffusive behavior is a consequence of employing a small TVD limiter value in the simulations. This choice aligns with the observation of a diffuse interface in the wicking experiments. Conversely, simulations using a larger TVD limiter value would have resulted in a sharper delineation of the liquid interface.

Tree-shaped networks are characterized by a hierarchical structure. An initial segment (bottom segment) bifurcates into two daughter segments (middle segments), and each daughter segment further splits into two channels (top segments). As shown in Fig. 9, the geometry is symmetric around the y axis. As a result, the fluid spreads evenly through the inner channels (channel 2). This is also evident in the wicking in the outer channels (channel 1). After about 70 s, the figure shows that the wicking in Tree2 membrane progresses to the end of channel 2, while this time is 80 s for channel 1. This phenomenon can be attributed to the closer proximity of the middle segment to channel 2. This allows the wicking fluid to enter channel 2 before reaching channel 1, resulting in the observed difference in wetting times. This observation highlights the influence of channel arrangement on wicking behavior within these geometries since other parameters such as length or width ratios remain identical for both inner and outer channels.

As evident in Fig. 10, the liquid fronts in the outer branches advance faster than those in the inner branches. This phenomenon can be attributed to the narrower inlet of the inner branches, which restricts fluid inflow and consequently leads to a longer wicking time. In contrast, Fig. 11 depicts wider inlets for the inner channels, resulting in comparable advancement of the liquid fronts across all branches.

The results for the wicking length as a function of time within the tree-shaped and multiplexed membranes are shown in Fig. 12. Due to the symmetric geometry of the profiles around the y-axis (see Fig. 8), only the liquid fronts in the bottom segment and the left middle segment and then in channels 1 and 2 of each profile need to be plotted. Consequently, the vertical coordinates of the liquid fronts in all these segments are monitored to represent the wicking length.

The results demonstrate a higher wicking velocity at the initial stages of the process for all investigated geometries. This behavior persists until the liquid front reaches the first bifurcation point for each geometry, with these points potentially exhibiting variations in vertical position. Beyond these points, distinct features emerge in the wicking curves.

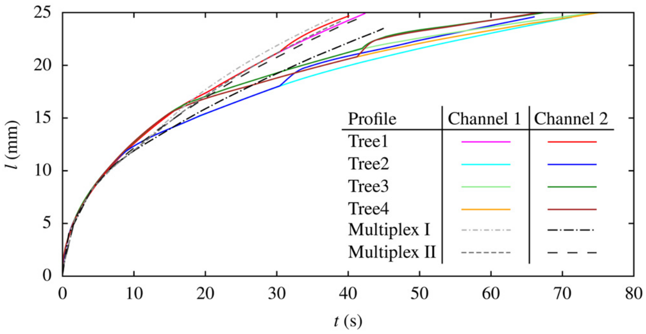

FIG. 12. Wicking length over time for the tree-shaped membranes from Table V and multiplexed membranes designed by *Sartorius*.

Among the geometries studied, the outer branches (channel 1) of multiplex I display the fastest wicking. This is due to two factors: the shorter fluid path through the 25 mm membrane and the wider inflow segment, characteristics not shared by the inner branches (channel 2). Notably, the difference in wicking times between channels 1 and 2 in multiplex II is less pronounced compared to multiplex I.

Within the tree-shaped geometries, Tree1 exhibits the fastest imbibition, comparable to the wicking processes observed in both multiplexed LFAs. Conversely, Tree2, Tree3, and Tree4 exhibit slower wicking processes due to the requirement for the wicking liquid to traverse longer membranes.

As noted earlier in this section and illustrated in Fig. 12, wicking in channel 2 of tree-shaped membranes is generally faster than in channel 1. This phenomenon is due to the closer proximity of the middle segment to channel 2, which gives the wicking liquid preferential access compared to channel 1. This observation suggests a valuable design strategy. By strategically manipulating the arrangement of branches within a tree-shaped network, wicking velocity can be tailored to optimize device performance for a specific application.

3. Wicking in membranes with asymmetric branches

Up to this point, the investigations have focused on wicking processes in membranes with branches that exhibit symmetry around the vertical axis. To elucidate the influence of asymmetry on wicking behavior, the 2D wicking simulation is repeated for a modified tree-shaped network based on the Hess–Murray law. This modified network is generated by removing the right inner channel from the previously studied symmetric design. The resulting visualizations of fluid propagation within this asymmetric network are presented in Fig. 13.

As can be seen, the fluid front shows different evolutions through the asymmetric channels. When labeled from the left, as shown in Fig. 13(a), the wicking in the right channel (channel 3) progresses faster. This is due to two factors: the absence of a bifurcation in the right middle segment and the reduced total pore space compared to the total pore space of channels 1 and 2. In simpler terms, all incoming fluid from the right middle segment can wet the membrane in channel 3 more quickly. This behavior is in contrast to the observations for the

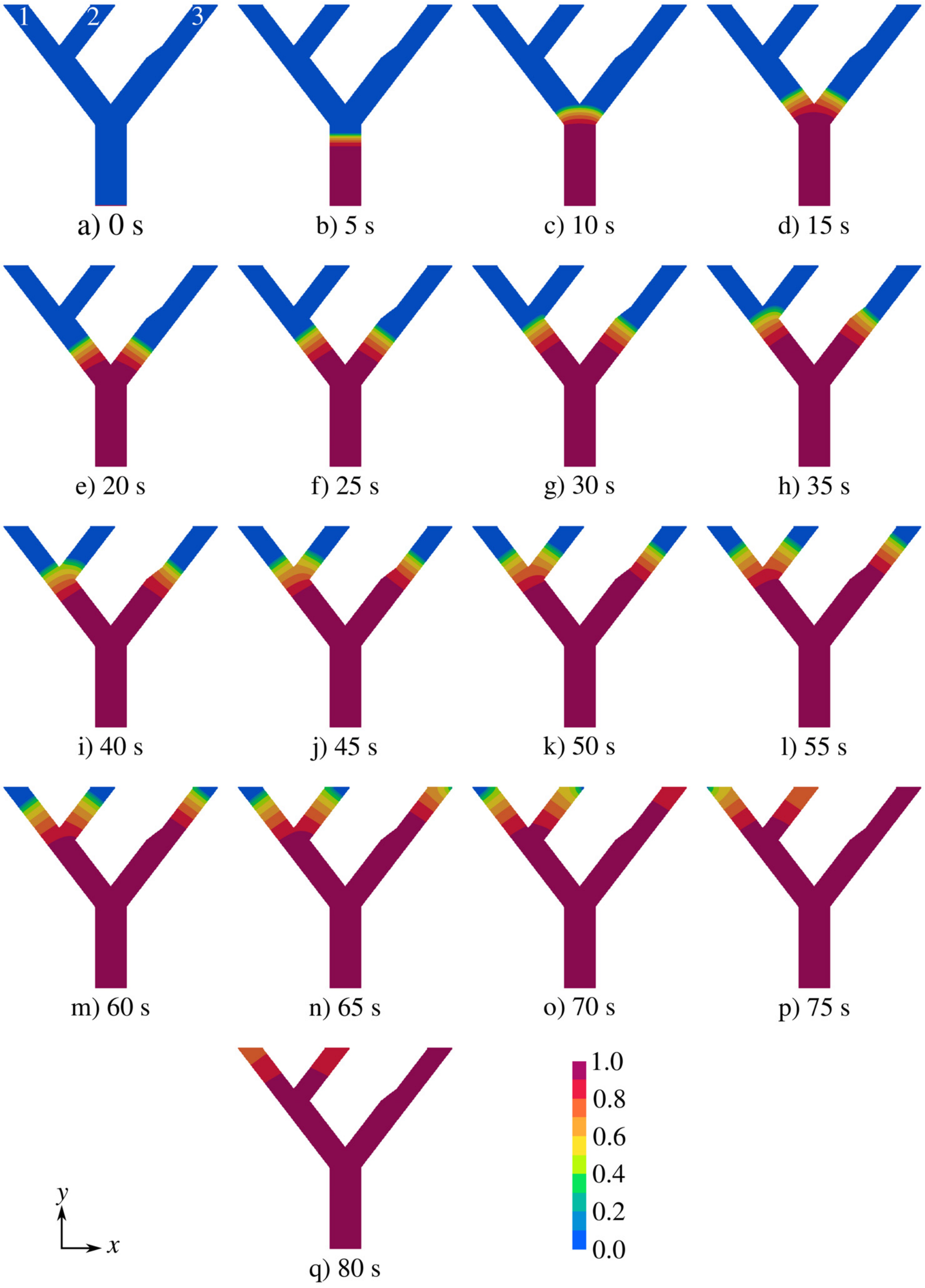

FIG. 13. The wetting phase (water) saturation in the asymmetric Tree2 membrane profile from Table V, where the evolution is displayed every 5 s.

symmetric membrane based on the Hess–Murray law, as shown in Fig. 9, where wicking in the outer channels takes longer. However, consistent with the findings for symmetric tree-shaped membranes, wicking in channel 2 remains faster than in channel 1 due to the closer proximity of the middle segment to channel 2. The observations in this section highlight that not only does the arrangement of the channels influence wicking behavior, but the presence of asymmetry also plays a significant role.

Figure 14 depicts the evolution of the wicking fronts within the channels of the asymmetric tree-shaped membrane as a function of time. Due to the asymmetry, data for all three liquid fronts are presented for comparative analysis. The figure reveals a faster movement of the wetting fluid across the membrane in the early stages. The wicking curves for channels 1 and 2 show identical behavior before reaching the bifurcation point where the liquid splits. However, because channel 2 is closer to the incoming fluid, it exhibits a higher wetting

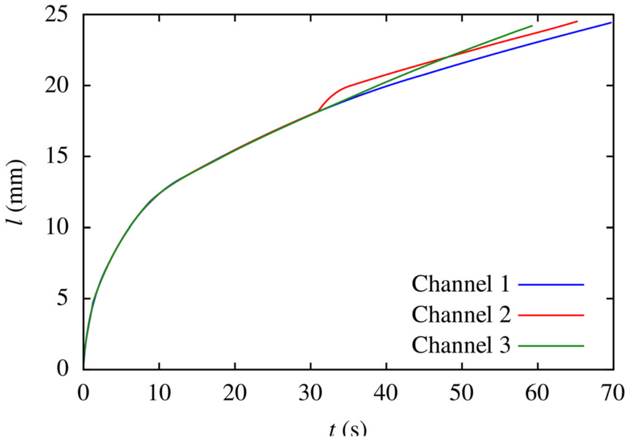

FIG. 14. Wicking length over time for the asymmetric Tree2 membrane from Table V.

phase saturation earlier than channel 1. Within channel 3, the fluid movement initially mirrors channels 1 and 2 until just over 30 s. Notably, the wicking front in channel 3 surpasses that of channel 2 shortly before reaching 50 s.

B. Influence of membrane type on wicking in multi-branch membranes

This section investigates the influence of membrane type on the wicking behavior in multiplexed LFAs designed by *Sartorius* (see Fig. 8). Two different membrane types from Table I are selected for wicking simulations using the IMPES solver in PACE3D. The simulation setup replicates that used in Sec. III A 2 for consistency. Due to the symmetry of the geometries around the *y*-axis, only the liquid fronts within an outer channel (channel 1) and an inner channel (channel 2) are captured for analysis. Figure 15 presents the wicking curves for these channels in both membrane types A (dashed lines) and B (solid lines).

As expected, the wicking trends observed for membrane type B are similar to those for type A. However, the wicking process is significantly slower for membrane type B due to its lower permeability. Furthermore, when using the same membrane type but different designs (multiplex I and II), the geometric factors cause the disparity between the wicking curves of the two channels. For example, in the case of membrane type A, the difference in wicking times between channels 1 and 2 is less pronounced in multiplex II compared to multiplex I. This observation is also true for membrane type B. Interestingly, a comparison of the wicking curves for different membrane types shows that the choice of membrane material can either increase or decrease the existing discrepancies in wicking behavior between channels. Using this knowledge, it becomes possible to manipulate or control the wicking behavior not only by geometric design but also by strategic selection of different membrane types.

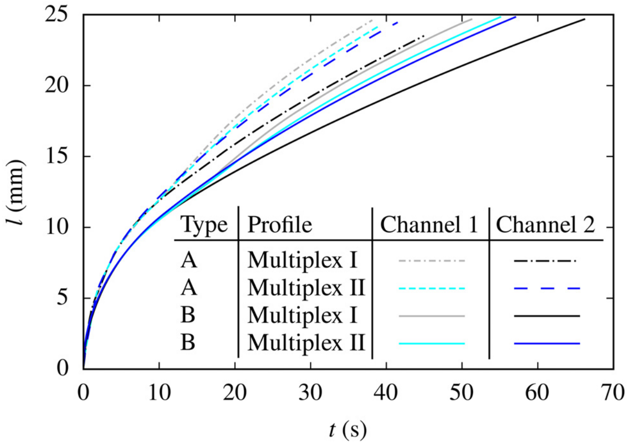

FIG. 15. Wicking length over time for the multiplexed membranes designed by *Sartorius* with the membrane types from 1.

IV. CONCLUSION

In the present study, a multi-scale modeling framework was developed to investigate capillary-driven fluid dynamics in polymeric porous membranes employed in lateral flow assays (LFAs). The framework incorporates microscopic characteristics of the membranes into a macroscopic, two-phase flow model, leading to a comprehensive understanding of wicking phenomena in LFAs. The model explicitly accounts for the complex interactions between the permeating and displaced fluids within the porous structure, providing a refined representation of the wicking process.

Utilizing the implicit pressure explicit saturation (IMPES) algorithm, the two-phase model captures both microstructural and macroscopic influences on fluid flow. The effectiveness of the model has been rigorously validated against established literature and experimental data, demonstrating its reliability for simulating fluid transport across various membrane configurations. To the best of our knowledge, the approach proposed in this study represents a novel numerical modeling technique for investigating the wicking process within multiplexed LFAs. This innovative framework offers a comprehensive approach to study the wicking process within membranes of arbitrary profiles and with different membrane properties. This is a significant step forward in the field of LFA research.

A quantitative analysis of the wicking process in Y-shaped and multi-branch membranes was performed by tracking the vertical progression of the liquid fronts (wicking length), which quantifies the extent of liquid advancement within the channels. The results show a significant influence of the branching angle on the wicking dynamics

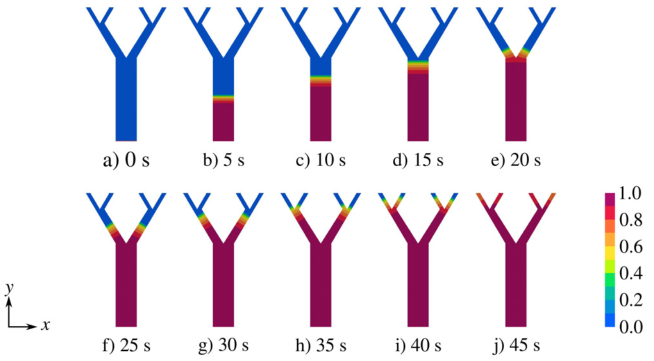

FIG. 16. The wetting phase (water) saturation in Tree1 membrane profile from Table V, where the evolution is displayed every 5 s.

in Y-shaped membranes. For instance, a membrane with a vertical length of 25 cm requires approximately 41 s to wick when the branching angle is 60° (Y1 profile). However, this value increases to approximately 101 s for a branching angle of 135° (Y6 profile).

Four-branch membranes are advantageous for multiplexed LFAs involving four tests. These membranes exhibit different wicking times for a vertical length of 25 cm. For example, Tree1 profile requires only about 40 s for complete wicking, while Tree2, Tree3, and Tree4 require more than 65 s. For four-branch membranes, the wicking velocity exhibits an inverse relationship with the inflow entrance width. These findings are crucial for the design of multiplexed LFAs, as they inform the consideration of factors such as length ratio, width ratio, branching angle, bifurcation point location, and inflow entrance dimensions, along with asymmetry and membrane type.

The results of this study enable the manipulation of wetting behavior within lateral flow assays (LFAs). By leveraging the acquired

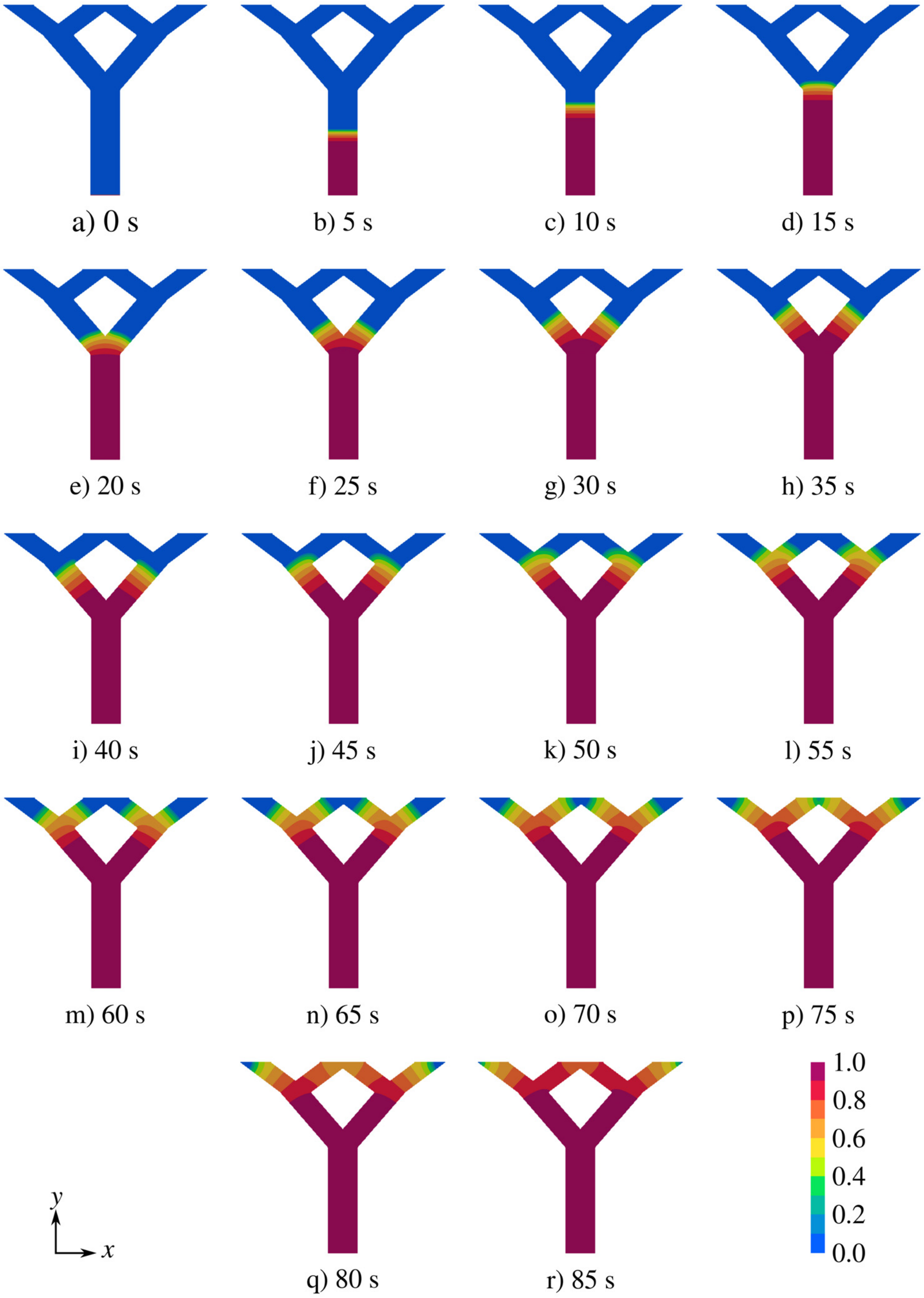

FIG. 17. The wetting phase (water) saturation in Tree3 membrane profile from Table V, where the evolution is displayed every 5 s.

data, precise control over wetting characteristics can be achieved, thereby enhancing LFA performance and reliability.

ACKNOWLEDGMENTS

This work was supported by the German government through the BMBF project MultiPore (Project ID: 13FH020KX0). The second author expresses gratitude for the support of the BMBF project ProStrom (Project ID: 03ETB026). The fourth author, Britta Nestler, acknowledges funding by the Helmholtz association within the program "MSE", No. 43.31.01.

AUTHOR DECLARATIONS

Conflict of Interest

The authors have no conflicts to disclose.

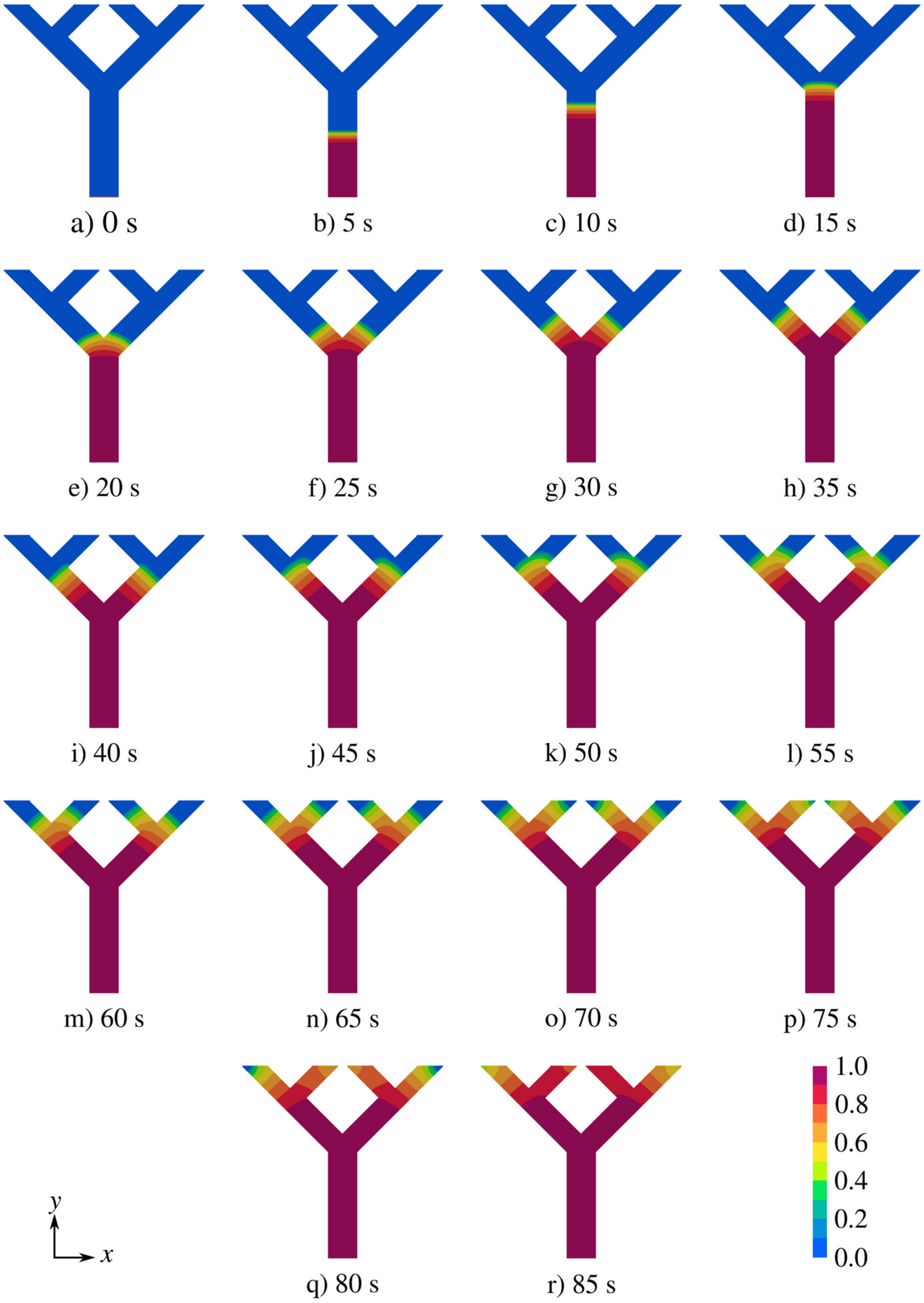
a) 0 s
b) 5 s
c) 10 s
d) 15 s
e) 20 s
f) 25 s
g) 30 s
h) 35 s
i) 40 s
j) 45 s
k) 50 s
l) 55 s
m) 60 s
n) 65 s
o) 70 s
p) 75 s
q) 80 s
r) 85 s

FIG. 18. The wetting phase (water) saturation in Tree4 membrane profile from Table V, where the evolution is displayed every 5 s.

Author Contributions

Farshid Jamshidi: Conceptualization (lead); Investigation (lead); Methodology (equal); Validation (equal); Visualization (lead); Writing – original draft (lead). **Siamak Bayat:** Methodology (equal); Validation (equal); Writing – review & editing (supporting). **Andrea Ernst:** Resources (lead); Writing – review & editing (supporting). **Britta Nestler:** Funding acquisition (lead); Supervision (lead); Writing – review & editing (supporting).

DATA AVAILABILITY

The data that support the findings of this study are available from the corresponding author upon reasonable request.

APPENDIX A: BOND NUMBER

To assess the relative influence of gravitational forces compared to surface tension forces, the Bond Number (Bo) is expressed as

$$Bo = \frac{\rho_{\mathrm{L}} g h}{\gamma_{\mathrm{LG}}/r_{\mathrm{p}}}. \tag{A1}$$

The properties of water/*Porefil*® as the liquid phase and air as the gas phase can be taken from Table II and the mean pore radius from Table I. When water is used as the wetting fluid and g is set to $9.8\,\mathrm{m\,s}^{-2}$, the Bond Numbers for membrane types A and B with a total length of $h = 0.04\,\mathrm{m}$ are found to be significantly less than 1 (0.0181 and 0.0169, respectively). This result indicates that gravitational forces are negligible compared to capillary forces. Conversely, when *Porefil*® is used as the wetting fluid, the Bond Numbers for membrane types A and B increase to 0.1082 and 0.1011, respectively. In these cases, gravitational forces must be taken into account.

APPENDIX B: WETTING IN TREE-SHAPED MEMBRANES

Figures 16–18 show how water saturation changes over time in tree-shaped membranes from Table V.

REFERENCES

[1] M. M. Gong and D. Sinton, "Turning the page: Advancing paper-based microfluidics for broad diagnostic application," Chem. Rev. **117**, 8447 (2017).

[2] S. Kasetsirikul, M. J. A. Shiddiky, and N.-T. Nguyen, "Challenges and perspectives in the development of paper-based lateral flow assays," Microfluid. Nanofluid. **24**, 17 (2020).

[3] J. Li and J. Macdonald, "Multiplexed lateral flow biosensors: Technological advances for radically improving point-of-care diagnoses," Biosens. Bioelectron. **83**, 177 (2016).

[4] L. Anfossi, F. D. Nardo, S. Cavalera, C. Giovannoli, and C. Baggiani, "Multiplex lateral flow immunoassay: An overview of strategies towards high-throughput point-of-need testing," Biosensors **9**, 2 (2019).

[5] F. Jamshidi, W. Kunz, P. Altschuh, M. Bremerich, R. Przybylla, M. Selzer, and B. Nestler, "Geometric flow control in lateral flow assays: Macroscopic single-phase modeling," Phys. Fluids **34**, 062110 (2022).

[6] S. Patari and P. S. Mahapatra, "Liquid wicking in a paper strip: An experimental and numerical study," ACS Omega **5**, 22931 (2020).

[7] D. Das, T. Singh, I. Ahmed, M. Masetty, and A. Priye, "Effects of relative humidity and paper geometry on the imbibition dynamics and reactions in lateral flow assays," Langmuir **38**, 9863 (2022).

[8] P. Altschuh, "Skalenübergreifende analyse makroporöser membranen im kontext digitaler zwillinge," Ph.D. thesis (Karlsruhe Institute of Technology (KIT), 2020).

[9] J. Hötzer, A. Reiter, H. Hierl, P. Steinmetz, M. Selzer, and B. Nestler, "The parallel multi-physics phase-field framework Pace3D," J. Comput. Sci. **26**, 1–12 (2018).

[10] F. Jamshidi, W. Kunz, P. Altschuh, T. Lu, M. Laqua, A. August, F. Löffler, M. Selzer, and B. Nestler, "A 3D computational method for determination of pores per inch (PPI) of porous structures," Mater. Today Commun. **34**, 105413 (2023).

[11] R. Masoodi, K. M. Pillai, and P. P. Varanasi, in *Fluids Engineering Division Summer Meeting*, Volume 1: Symposia, Parts A and B (ASME, 2008), pp. 251–259.

[12] R. Masoodi and K. Pillai, "A general formula for capillary suction-pressure in porous media," J. Porous Media **15**, 775 (2012).

[13] P. Altschuh, W. Kunz, M. Bremerich, A. Reiter, M. Selzer, and B. Nestler, "Wicking in porous polymeric membranes: Determination of an effective capillary radius to predict the flow behavior in lateral flow assays," Membranes **12**, 638 (2022).

[14] N. Fries, *Capillary Transport Processes in Porous Materials - Experiment and Model* (Cuvillier Verlag, Göttingen, 2010).

[15] R. Masoodi, K. M. Pillai, and P. P. Varanasi, "Darcy's law-based models for liquid absorption in polymer wicks," Am. Inst. Chem. Eng. AIChE J. **53**, 2769 (2007).

[16] C. Redondo, G. Rubio, and E. Valero, "On the efficiency of the IMPES method for two phase flow problems in porous media," J. Pet. Sci. Eng. **164**, 427 (2018).

[17] P. Bastian, "Numerical computation of multiphase flows in porous media," Habilitation thesis (Christian-Albrecht University of Kiel, 1999).

[18] T. Ahmed and T. Ahmed, in *Reservoir Engineering Handbook*, 4th ed. (Gulf Professional Publishing, Boston, MA, 2010), pp. 189–287.

[19] P. Horgue, C. Soulaine, J. Franc, R. Guibert, and G. Debenest, "An open-source toolbox for multiphase flow in porous media," Comput. Phys. Commun. **187**, 217 (2015).

[20] R. Brooks and A. Corey, *Hydraulic Properties of Porous Media*, Colorado State University Hydrology Paper (Colorado State University, 1964).

[21] X. Lu, A. Kharaghani, H. Adloo, and E. Tsotsas, "The Brooks and Corey capillary pressure model revisited from pore network simulations of capillarity-controlled invasion percolation process," Processes **8**, 1318 (2020).

[22] J. Niessner, *The Role of Interfacial Areas in Two-Phase Flow in Porous Media: Bridging Scales and Coupling Models* (University of Stuttgart, 2010).

[23] A. Bejan and S. Lorente, "Constructal theory of generation of configuration in nature and engineering," J. Appl. Phys. **100**, 041301 (2006).

[24] A. Bejan and S. Lorente, "The constructal law and the evolution of design in nature," Phys. Life Rev. **8**, 209 (2011).

[25] A. F. Miguel and L. A. Rocha, *Tree-Shaped Fluid Flow and Heat Transfer* (Springer Cham, 2018).

[26] A. F. Miguel, "Toward an optimal design principle in symmetric and asymmetric tree flow networks," J. Theor. Biol. **389**, 101 (2016).

[27] A. F. Miguel, "A general model for optimal branching of fluidic networks," Physica A **512**, 665 (2018).

[28] A. F. Miguel, "Constructal branching design for fluid flow and heat transfer," Int. J. Heat Mass Transfer **122**, 204 (2018).

[29] X. Zhang and S. Lorente, "Capillary trees for passively pumping water," J. Phys. D **55**, 165503 (2022).

[30] W. R. Hess, "Über die periphere Regulierung der Blutzirkulation," Pflüger's Arch. Gesamte Physiol. Menschen Tiere **168**, 439 (1917).

[31] C. D. Murray, "The physiological principle of minimum work," Proc. Natl. Acad. Sci. **12**, 207 (1926).

[32] E. Sciubba, "A critical reassessment of the Hess–Murray law," Entropy **18**, 283 (2016).

[33] V. R. Pepe, L. A. O. Rocha, and A. F. Miguel, in *Proceedings of the Constructal Law Conference 2017*, edited by A.-M. Morega and S. Lorente (The Publishing House of the Romanian Academy, Bucharest, Romania, 2017), pp. 444–455.

[34] D. Shou, L. Ye, and J. Fan, "Treelike networks accelerating capillary flow," Phys. Rev. E **89**, 053007 (2014).

[35] A. Bejan, L. Rocha, and S. Lorente, "Thermodynamic optimization of geometry: T- and Y-shaped constructs of fluid streams," Int. J. Therm. Sci. **39**, 949 (2000).

[36] B. Soni, A. F. Miguel, and A. Kumar Nayak, "A mathematical analysis for constructal design of tree flow networks under unsteady flow," Proc. R. Soc. A **476**, 20200377 (2020).

[37] A. Sehn, V. d. R. Pepe, A. F. Miguel, F. Zinani, and L. A. O. Rocha, in XXXVIII Ibero-Latin American Congress on Computational Methods in Engineering (2017).

[38] A. F. Miguel, "Fluid flow in a porous tree-shaped network: Optimal design and extension of Hess–Murray's law," Physica A **423**, 61 (2015).

[39] S. Lorente and A. Bejan, "Heterogeneous porous media as multiscale structures for maximum flow access," J. Appl. Phys. **100**, 114909 (2006).